Journal of Energy Chemistry 71 (2022) 547–561

Contents lists available at ScienceDirect

Journal of Energy Chemistry

journal homepage: www.elsevier.com/locate/jechem

http://www.journals.elsevier.com/journal-of-energy-chemistry/

Optimizing the oxide support composition in Pr-doped CeO_2 towards highly active and selective Ni-based CO_2 methanation catalysts

Anastasios I. Tsiotsias [a], Nikolaos D. Charisiou [a], Ayesha AlKhoori [b,c], Safa Gaber [b,c], Vlad Stolojan [d], Victor Sebastian [e,f,g], Bart van der Linden [h], Atul Bansode [h], Steven J. Hinder [i], Mark A. Baker [i], Kyriaki Polychronopoulou [b,c,i], Maria A. Goula [a,*]

[a] Laboratory of Alternative Fuels and Environmental Catalysis (LAFEC), Department of Chemical Engineering, University of Western Macedonia, GR-50100, Greece
[b] Department of Mechanical Engineering, Khalifa University of Science and Technology, Abu Dhabi, P.O. Box 127788, United Arab Emirates
[c] Center for Catalysis and Separations, Khalifa University of Science and Technology, Abu Dhabi, P.O. Box 127788, United Arab Emirates
[d] Advanced Technology Institute, Department of Electrical and Electronic Engineering, University of Surrey, Guildford GU2 4DL, UK
[e] Department of Chemical Engineering and Environmental Technology, Universidad de Zaragoza, Campus Río Ebro-Edificio I+D, 50018 Zaragoza, Spain
[f] Instituto de Nanociencia y Materiales de Aragón (INMA), Universidad de Zaragoza- CSIC, c/ María de Luna 3, 50018 Zaragoza, Spain
[g] Networking Research Center on Bioengineering, Biomaterials and Nanomedicine, CIBERBBN, 28029 Madrid, Spain
[h] Department of Chemical Engineering, Delft University of Technology, Van der Massweg 9, 2629 HZ Delft, The Netherlands
[i] The Surface Analysis Laboratory, Faculty of Engineering and Physical Sciences, University of Surrey, Guildford GU2 4DL, UK

ARTICLE INFO

Article history:
Received 26 November 2021
Revised 24 March 2022
Accepted 1 April 2022
Available online 11 April 2022

Keywords:
Power-to-gas
CO_2 methanation
Ni-based catalyst
Pr-doped CeO_2
Oxygen vacancy
Catalytic activity
Activation energy

ABSTRACT

In this study, Ni catalysts supported on Pr-doped CeO_2 are studied for the CO_2 methanation reaction and the effect of Pr doping on the physicochemical properties and the catalytic performance is thoroughly evaluated. It is shown, that Pr^{3+} ions can substitute Ce^{4+} ones in the support lattice, thereby introducing a high population of oxygen vacancies, which act as active sites for CO_2 chemisorption. Pr doping can also act to reduce the crystallite size of metallic Ni, thus promoting the active metal dispersion. Catalytic performance evaluation evidences the promoting effect of low Pr loadings (5 at% and 10 at%) towards a higher catalytic activity and lower CO_2 activation energy. On the other hand, higher Pr contents negate the positive effects on the catalytic activity by decreasing the oxygen vacancy population, thereby creating a volcano-type trend towards an optimum amount of aliovalent substitution.

1. Introduction

The dreadful effects that anthropogenic climate change will have on ecosystems and human societies alike has led to a spike of research interest in carbon capture and utilization (CCU) technologies [1]. Furthermore, safety concerns, as well as the high costs and material requirements associated with H_2 storage and transportation motivates the search for alternative energy-rich molecules (energy buffers) to apply in the so-called "Power-to-Gas" processes [2,3]. The CO_2 methanation reaction (Eq. (1)) attempts to tackle both problems, by utilizing CO_2 captured from flue gases of conventional fossil-fuel powered units and green H_2 produced via electrolysis using electricity harnessed from renewable sources, into CH_4 or synthetic natural gas [4–6].

$$CO_2 + 4H_2 \rightarrow CH_4 + 2H_2O \quad (1)$$

CH_4 is a gas with a much higher volumetric energy density than H_2 (by a factor of 3.2 at any given pressure [7]), can be easily stored and transported and thus constitutes a perfect candidate as an energy buffer for storing intermittent renewable energy [3,4]. CO_2 emitted from the combustion of synthetic natural gas is compensated by the initial CO_2 capture step, thus creating a closed carbon process with net zero CO_2 emissions [4,6].

The most common metals that can catalyze the transformation of CO_2 and H_2 into CH_4 are Rh, Ru and Ni [8–10]. Rh and Ru are precious (or noble) metals and thus Rh- and Ru-based catalysts are associated with much higher costs compared to Ni-based ones, which makes them unsuitable for industrial implementation [10].

* Corresponding author.
E-mail address: mgoula@uowm.gr (M.A. Goula).

https://doi.org/10.1016/j.jechem.2022.04.003

Although the metallic Ni surface alone is generally fairly active towards catalyzing the CO_2 methanation reaction [11], the choice of the metal oxide support in Ni catalysts can drastically impact the catalytic activity [12]. Ni/CeO_2-type catalysts are considered to be by far the most active and selective catalysts for CO_2 methanation, compared to Ni catalysts supported on other types of supports (e.g., Al_2O_3 or SiO_2), a property attributed to the great oxygen mobility of the CeO_2 support, which originates from its rich defect chemistry ($Ce^{4+} \leftrightarrow Ce^{3+}$ cycle) [8,9,13]. Cárdenas-Arenas et al. [14] have indicated that the CO_2 methanation mechanism over Ni/CeO_2 differs from Ni/Al_2O_3, with Ni/CeO_2 exhibiting different sites for H_2 (metallic Ni surface) and CO_2 (NiO-CeO_2 interface) dissociation, while also being able to transport oxygen species throughout the CeO_2 lattice and thereby not blocking the catalytically active sites. Therefore, the use of a CeO_2-based support is often considered essential in order to guarantee a sufficient catalytic activity for Ni-based catalysts [8–10,13,14].

The beneficial contribution of defect sites and especially oxygen vacancies that are located at the support surface during the CO_2 methanation reaction has been addressed by numerous works in the literature [15–19]. Therefore, a rational strategy to improve the CO_2 methanation performance of Ni/CeO_2 catalysts would be to try to increase the oxygen vacancy population in the CeO_2 support [16]. This can most notably be achieved via aliovalent substitution of Ce^{4+} cations in the CeO_2 lattice with other metal cations of lower valence, e.g., Y^{3+}, La^{3+}, Pr^{3+} or Sm^{3+} [16,18,19]. Pr can readily dissolve into the crystalline lattice of CeO_2 and, like Ce, can adopt both +4 and +3 oxidation states, the difference being that Pr^{4+} reduces far easier to Pr^{3+} compared to the $Ce^{4+} \rightarrow Ce^{3+}$ transition [20,21]. Therefore, it has been reported that Pr doping of CeO_2 up to around 10 at%–20 at% (x = 0.1–0.2 in $Ce_{1-x}Pr_xO_{2-\delta}$ solid solutions) can greatly enhance the population of oxygen vacancies and oxygen uptake of the mixed oxide [20]. The substitution of Ce^{4+} cations in the CeO_2 lattice with Pr^{3+} ones can be described by the following Kröger-Vink equation (Eq. (2)):

$$Pr_2O_3(CeO_2) \rightarrow 2Pr'_{Ce} + V_O + 3O^x_O \quad (2)$$

Pr-doped CeO_2 oxides have been applied in many catalytic applications, either as stand-alone oxidation catalysts, or as oxide supports for other metal-based catalysts (e.g., Ni). Zhang et al. [22] employed Pr-doped CeO_2 in the Prins condensation-hydrolysis of isobutene with formalin and noted that the increased population of surface oxygen vacancies, which peaked for a Pr/(Pr + Ce) atomic ratio of 0.2, promoted the catalytic performance via enhancing the adsorption of HCHO. Regarding Ni/Pr-CeO_2 catalysts, Makri et al. [23] found that an enhanced transfer of lattice oxygen species in Pr-doped CeO_2 could promote carbon gasification during the dry reforming of methane, whereas Xiao et al. [24] reported that Pr doping of CeO_2 up to 20 at% could increase the oxygen vacancy population, decrease the crystallite size of Ni and thereby improve the catalytic activity, stability and coking resistance during the steam reforming of ethanol. Concerning the CO_2 methanation reaction, Siakavelas et al. [18,19] prepared Ni catalysts supported on CeO_2 and La_2O_3-CeO_2, modified with Mg, Sm and Pr (10 at%) and showed that the increase in the population of surface oxygen vacancies (especially upon Pr modification) was the property that led to the rise in catalytic activity. Finally, Rodriguez et al. [25] investigated the effect of Pr content on Ru/CeO_2 catalysts and found that a low Pr loading (3 wt%) had a positive influence during CO_2 methanation by enhancing the oxygen mobility of the CeO_2 support, whereas high Pr loadings (25 wt%) negatively impacted the initial chemisorption and dissociation of CO_2, which takes place at the Ru-CeO_2 interface.

This work investigates the effect of the Pr content in the CeO_2 support of Ni-based catalysts, which to the best of our knowledge has not yet been studied for the CO_2 methanation reaction. To examine the physicochemical properties of the mixed metal oxide supports and reduced catalysts, a multitude of characterization methods is employed, namely X-ray diffraction (XRD), N_2 physisorption, H_2-temperature-programmed reduction (H_2-TPR), CO_2-temperature programmed desorption (CO_2-TPD), H_2-TPD, Raman spectroscopy, X-ray photoelectron spectroscopy (XPS), transmission electron microscopy (TEM), high-angle annular dark field scanning transmission electron microscopy (HAADF-STEM) and energy dispersive X-ray spectroscopy (EDS). Catalytic performance is evaluated at the temperature region of 200–500 °C and the CO_2 activation energy of the catalysts is calculated. The catalytic stability is evaluated under 24 h time-on-stream experiments and the spent catalysts are investigated to examine potential degradation effects (e.g., carbon deposition or nanoparticle sintering). Moreover, the reaction pathway is investigated via in-situ diffuse reflectance infrared Fourier transform spectroscopy (DRIFTS) experiments.

2. Experimental

2.1. Catalyst preparation

Pr-doped CeO_2 oxide supports ($Ce_{1-x}Pr_xO_{2-\delta}$, x = 0, 0.05, 0.1, 0.2, 0.5) were prepared via the citrate sol–gel method. Calculated amounts of $Ce(NO_3)_3{\cdot}6H_2O$ (Sigma-Aldrich, 99%) and $Pr(NO_3)_3{\cdot}6H_2O$ (Sigma-Aldrich, 99.9%) were initially dissolved in 100 mL of d-H_2O under stirring. Citric acid (Fluka, 99.5%) was then introduced to the metal nitrate aqueous solution at a molar ratio of citric acid to total metal cations equal to 1.5. The solution was then heated up at 80 °C until the evaporation of water led to the formation of a green and viscous gel-like syrup, which was then left to dry at 130 °C overnight. The resulting citrate gel was crushed in a mortar and then calcined at 400 °C for 1 h to combust the organic components and finally at 500 °C for 4 h. The prepared supports were named as PrXCe, where X is the nominal at% content of Pr in the CeO_2 supports (e.g., Pr10Ce corresponds to 10 at% Pr in CeO_2 or to $Ce_{0.9}Pr_{0.1}O_{2-\delta}$).

Ni was introduced in the prepared supports via wet impregnation. In short, a calculated amount of $Ni(NO_3)_2{\cdot}6H_2O$ (Fluka, 97%), in order to obtain a final Ni loading of 10 wt%, was dissolved in 100 mL of d-H_2O under stirring, followed by the addition of the corresponding support. Water evaporation took place in a rotary evaporator at 72 °C, the resulting slurry was dried at 130 °C overnight and finally calcined at 400 °C for 4 h under static air. The catalysts prepared this way were denoted as "calcined" and named as NiO/PrXCe. To obtain their reduced counterparts, the calcined catalysts were reduced at 500 °C for 1 h under a H_2 flow and were named as Ni/PrXCe.

2.2. Catalyst characterization

Detailed information concerning the characterization techniques employed in this work, including instruments and methodology, can be found in Refs. [18,19]. In short, the following characterization techniques were used: (i) XRD was employed for the identification of the crystalline structures in the supports and reduced catalysts. The d-spacing values, as well as the crystallite sizes of the various phases were determined using the Bragg equation and the Scherrer equation respectively. (ii) N_2 physisorption was used for the evaluation of the textural properties and the calculation of the Brunauer-Emmett-Teller (BET) surface area, pore volume and average pore width. (iii) H_2-TPR over was employed to investigate the reducibility of the materials. (iv) CO_2-TPD helped with the

determination of the surface basic properties. (vi) H_2-TPD was carried out to calculate the exposed Ni^0 surface area, which leads to the determination of the dispersion of the Ni active phase and the average size of Ni^0 nanoparticles. It should be noted, that H_2-TPR was conducted over the calcined catalysts (20% O_2/He, 500 °C, 2 h), whereas a reduction step was introduced before the CO_2-TPD and H_2-TPD experiments (H_2, 500 °C, 1 h). (vii) Raman spectroscopy was conducted to study the oxygen environment and especially the presence of oxygen vacancies. (vii) XPS analysis was used for the determination of the surface elements, as well as their chemical environment and oxidation state. Lastly, (viii) TEM, HAADF-STEM and EDS were carried out in order to obtain information about the morphology of the reduced catalysts and the elemental distribution. The catalyst was dispersed in Milli-Q water using ultrasounds and 25 μL were dropped and cast over a TEM 200-mesh copper grid with holey carbon film.

Regarding in-situ DRIFTS characterization, FTIR spectra were recorded on a Thermo Scientific Nicolet 8700 FTIR spectrometer equipped with a TRS-detector (LN-MCT) and a high-temperature DRIFT-cell with CaF_2 windows (HVC praying mantis Harrick). The spectra of the samples were measured accumulating 128 scans at a resolution 4 cm^{-1}, under a 25 mL min^{-1} flow of He (for flushing) or 80% H_2 in He (for catalyst reduction) or 16% CO_2 + 64% H_2 (hydrogenation reaction) in He. In a typical experiment, the catalyst powder was loaded in the reaction cell and reduced 500 °C for 1 h under 80% H_2 in He flow. After the reduction, the sample was cooled down in He flow to room temperature and a background was collected. The gases were then switched to the reaction mixture and spectra collection was carried out at different temperatures (150, 200, 250, 300, 350 and 400 °C).

2.3. Catalytic testing

Catalytic activity and stability tests were carried out at atmospheric pressure in a continuous flow fixed-bed quartz reactor (0.9 cm I.D.), using a cold trap at the reactor outlet in order to remove the produced water vapor. Before commencement of any experimental work, all the as-prepared (calcined) catalysts were in situ reduced at 500 °C for 1 h under a H_2 flow. Evaluation of the catalytic performance was carried out using three Experimental Protocols (#1, #2 and #3).

Evaluation of the catalytic activity as a function of reaction temperature under a relatively low weight hourly space velocity (WHSV) of 25000 mL g_{cat}^{-1} h^{-1} was performed under Experimental Protocol #1. 0.24 g of the catalyst, diluted with quartz sand till 0.5 g, were initially loaded into the quartz reactor. The total flow rate was set at 100 mL min^{-1} (10 mL min^{-1} CO_2, 40 mL min^{-1} H_2 and 50 mL min^{-1} Ar), while the reactor temperature was varied between 200 and 500 °C under 50 °C intervals and remained at each temperature step for 30 min to achieve steady-state operation. Under Experimental Protocol #2, the catalysts were tested under a higher WHSV of 100000 mL g_{cat}^{-1} h^{-1}, in a similar procedure to Experimental Protocol #1, the only difference being that a lower catalyst mass of 0.06 g was used and that extra temperature steps were introduced for every 10 °C between 250 and 350 °C. The CO_2 activation energy values were calculated under this experimental protocol, assuming pseudo-first order kinetics and for CO_2 conversions <20%, so as to avoid mass transfer limitations. Finally, in Experimental Protocol #3 the stability of the catalysts was evaluated during 24 h time-on-stream tests at a constant temperature of 400 °C (WHSV = 25000 mL $g_{cat}^{-1}h^{-1}$, same procedure as in Experimental Protocol #1).

The analysis of the gas composition at the reactor outlet was carried out online by gas chromatography, as described in Ref. [18]. CO was detected as the only reaction by-product besides CH_4. Deviations calculated from the carbon balance were found to be less than −2%. CO_2 conversion, CH_4 selectivity, CO selectivity and CH_4 yield were calculated based on the following Eqs. (3)–(6):

$$X_{CO_2}(\%) = \frac{C_{CH_4}^{out} + C_{CO}^{out}}{C_{CO_2}^{out} + C_{CH_4}^{out} + C_{CO}^{out}} 100, \quad (3)$$

$$S_{CH_4}(\%) = \frac{C_{CH_4}^{out}}{C_{CH_4}^{out} + C_{CO}^{out}} 100, \quad (4)$$

$$S_{CO}(\%) = \frac{C_{CO}^{out}}{C_{CH_4}^{out} + C_{CO}^{out}} 100, \quad (5)$$

$$Y_{CH_4}(\%) = \frac{X_{CO_2} \cdot S_{CH_4}}{100}, \quad (6)$$

where C^{out} represents the concentration of each gas at the reactor outlet.

Finally, the reaction rate for the consumption of CO_2, expressed in mol of CO_2 converted per catalyst mass and per second (mol g_{cat}^{-1} s^{-1}), was calculated via the following Eq. (7):

$$r_{CO_2} = \left(\frac{X_{CO_2}}{100}\right) \cdot \left(\frac{F_{CO_2}}{W_{cat}}\right), \quad (7)$$

where X_{CO_2} is the CO_2 conversion (%), F_{CO_2} is the CO_2 molar flow rate at the reactor inlet expressed in moles per second and W_{cat} is the mass of the catalyst used in grams.

3. Results and discussion

3.1. Evaluation of the catalytic performance

3.1.1. Catalytic performance as a function of reaction temperature

The CO_2 methanation performance of the prepared catalysts was first evaluated under Experimental Protocol #1, i.e., with a WHSV of 25000 mL $g_{cat}^{-1}h^{-1}$. The results regarding CO_2 conversion and CH_4 selectivity are presented in Fig. 1, whereas CH_4 yield can be found in Fig. S1. The dotted lines present in the graphs represent thermodynamic equilibrium calculations using Aspen Plus for ratio H_2:CO_2 = 4:1 and total pressure 1 atm. A comparison of the catalytic activity of the five prepared catalysts regarding their CO_2 conversion, CH_4 selectivity and CH_4 yield values is provided in Table 1.

Ni/Ce (without Pr doping) was found to be fairly active for the CO_2 methanation reaction. The doping of the CeO_2 support with 5 at% and 10 at% Pr acts to increase the catalytic performance both at low (200–300 °C) and at higher (350–500 °C) temperatures, with a concomitant increase in the selectivity for CH_4. Maximum CO_2 conversion for the best-performing Ni/Pr10Ce catalyst (Ni supported on CeO_2 modified with 10 at% Pr) is reached at 400 °C and lies at 72%, whereas the CO_2 conversion value at the same temperature for Ni/Ce is 65%. The corresponding CH_4 selectivity values at 400 °C lie at 98% and 96% for Ni/Pr10Ce and Ni/Ce respectively. However, when the Pr-content in the CeO_2 support is increased above 10 at%, the CO_2 methanation reactivity is negatively impacted. Ni/Pr20Ce (Ni supported on CeO_2 modified with 20 at% Pr) has a comparable performance to Ni/Ce, albeit with a slightly higher reactivity and CH_4 selectivity at low temperatures. When the extent of Pr-modification in CeO_2 reaches 50 at% (Ni/Pr50Ce), the CO_2 methanation activity drops even lower. A correlation between the catalysts' physicochemical properties and the CO_2

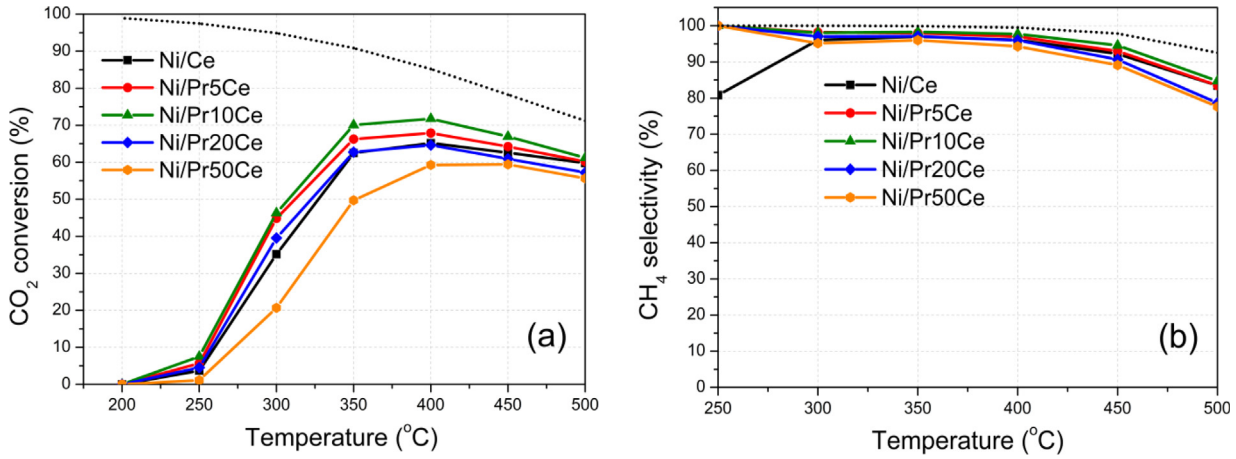

Fig. 1. Catalytic performance as a function of reaction temperature: (a) CO_2 conversion and (b) CH_4 selectivity. Reaction conditions: Experimental Protocol #1 (WHSV = 25000 mL $g_{cat}^{-1}h^{-1}$). The dotted lines represent thermodynamic equilibrium calculations using Aspen Plus for ratio H_2:CO_2 = 4:1 and total pressure 1 atm.

Table 1
Comparison of catalysts' CO_2 methanation activity at 400 °C, and at 300 °C in parentheses. Reaction conditions: Experimental Protocol #1.

Catalyst name	CO_2 conversion (%)	CH_4 selectivity (%)	CH_4 yield (%)
Ni/Ce	65 (35)	96 (96)	63 (34)
Ni/Pr5Ce	68 (45)	97 (98)	66 (44)
Ni/Pr10Ce	72 (46)	98 (98)	70 (45)
Ni/Pr20Ce	65 (40)	96 (97)	62 (38)
Ni/Pr50Ce	59 (21)	94 (95)	56 (20)

methanation catalytic performance is provided in a following section.

After the initial catalytic activity evaluation, temperature step experiments were carried out using a higher WHSV (100000 mL $g_{cat}^{-1}h^{-1}$) under Experimental Protocol #2, in order to construct Arrhenius plots and calculate the CO_2 activation energies of the catalysts (Fig. 2). As expected, and reported by other studies [26], the catalytic performance drops upon increasing the space

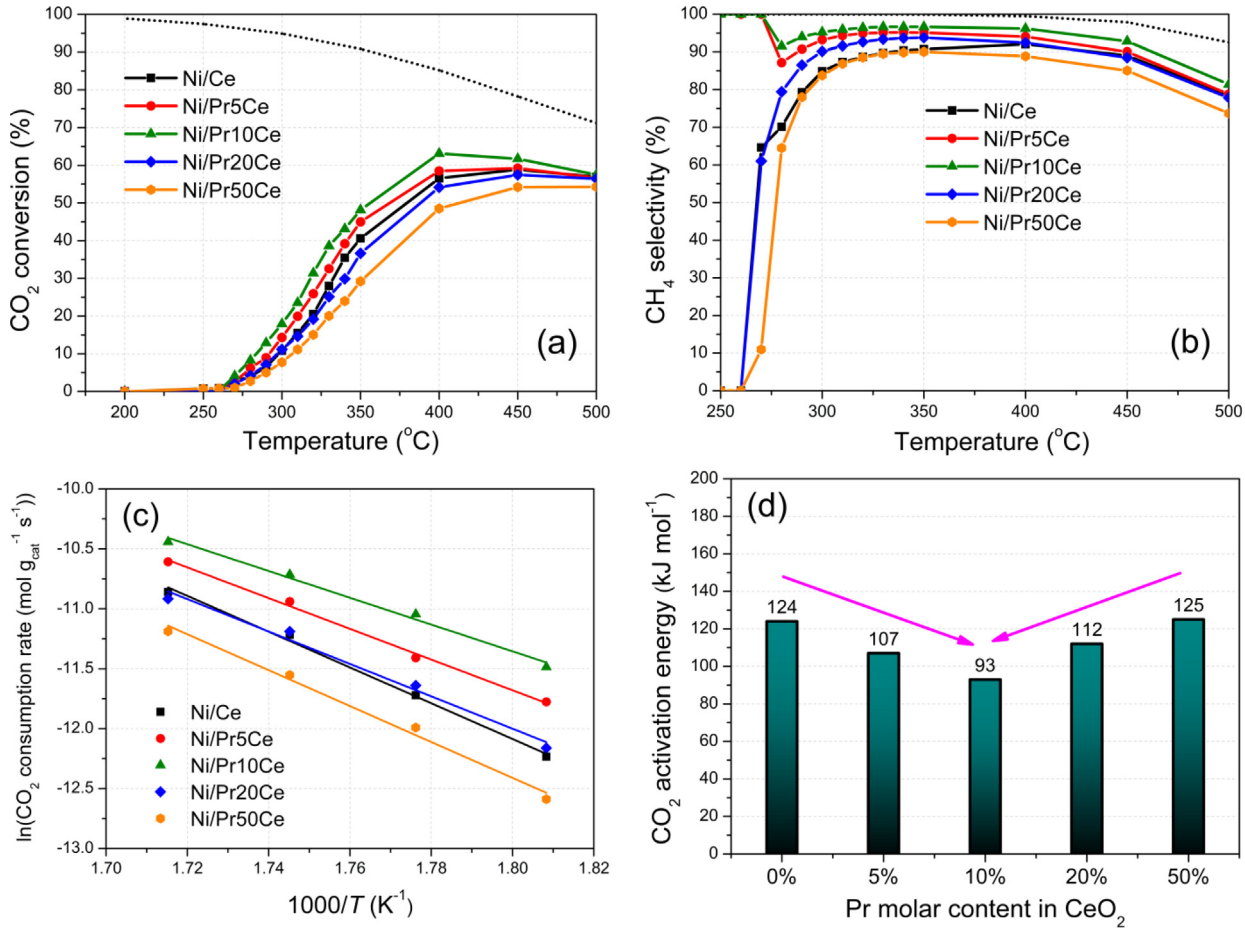

Fig. 2. Catalytic performance as a function of reaction temperature: (a) CO_2 conversion and (b) CH_4 selectivity. (c) Forward CO_2 consumption rates as a function of reciprocal temperature. (d) Calculated CO_2 activation energy for the catalysts with different at% Pr. Reaction conditions: Experimental Protocol #2 (WHSV = 100000 mL $g_{cat}^{-1}h^{-1}$). The dotted lines represent thermodynamic equilibrium calculations using Aspen Plus for ratio H_2:CO_2 = 4:1 and total pressure 1 atm.

velocity, due to the decreased contact time of the reactant gases with the catalytically active sites (Fig. 2a). CH_4 selectivity also drops upon increasing the WHSV in favor of CO selectivity, which is produced due to the side-reaction of reverse water–gas shift (RWGS) [26,27] (Fig. 2b). As an example, CO_2 conversion and CH_4 selectivity values at 400 °C for Ni/Pr10Ce lie at 63% and 96% when WHSV = 100000 mL $g_{cat}^{-1}h^{-1}$, compared to 72% and 98% respectively for WHSV = 25000 mL $g_{cat}^{-1}h^{-1}$. Nevertheless, the performance of the different catalysts follows the same trend, i.e., CO_2 methanation activity increases for the Ni catalysts supported on CeO_2 modified with 5 at% and 10 at% Pr, whereas the use of higher Pr-contents leads to a drop in the catalytic activity of the corresponding catalysts.

Arrhenius plots (Fig. 2c), i.e., plots of the natural logarithm of the CO_2 consumption rate as a function of reciprocal temperature, regarding the five catalysts were constructed. A gradual change between the slopes of the regression lines, and thus the activation energies, with regards to the Pr content in the catalysts is apparent. The CO_2 activation energies for the different catalysts are comparatively presented in Fig. 2(d). The CO_2 activation energy for the Ni/Ce catalyst (Ni supported on unmodified CeO_2) was calculated at 124 kJ mol^{-1}, which is close to the value reported by other works in the literature [28–30]. This value then dropped for the Ni/Pr5Ce and Ni/Pr10Ce catalysts to 107 and 93 kJ mol^{-1} respectively, before rising again for Ni/Pr20Ce and Ni/Pr50Ce catalysts to 112 and 125 kJ mol^{-1} respectively. Therefore, the CO_2 activation energy appears to follow an inverse-volcano trend as a function of Pr at% in CeO_2, with the lowest value corresponding to the catalyst whose support was modified with 10 at% Pr. It is thus concluded, that CO_2 activation proceeds easier on Ni/Pr10Ce, probably as a result of a higher number of CO_2 chemisorption sites (oxygen vacancies and Ni-O-Ce interfacial sites) [28,31], as will be explained later.

3.1.2. Catalytic performance as a function of reaction time

The catalytic stability of two representative catalytic systems, i.e., of the Ni-based catalyst supported on unmodified CeO_2 (Ni/Ce) and the most active Ni-based catalyst supported on 10 at% Pr-modified CeO_2 (Ni/Pr10Ce), was evaluated during 24 h time-on-stream tests at 400 °C under Experimental Protocol #3 (Fig. 3). In general, both catalysts appear to be quite stable, exhibiting only a minor loss of CO_2 conversion (7% for Ni/Ce and 6% for Ni/Pr10Ce), while CH_4 selectivity also remained stable (<1% drop for both catalysts). Ni/Pr10Ce was found to be more active and selective towards the production of CH_4 throughout the duration of the experiment compared to Ni/Ce, in agreement with the results obtained during the activity experiments. The final (steady-state) values for CO_2 conversion, CH_4 selectivity and CH_4 yield for Ni/Ce were 65%, 96% and 63% respectively, whereas the corresponding values for the most active Ni/Pr10Ce were 69%, 98% and 68% respectively.

3.2. Characterization of the supports, calcined and reduced catalysts

3.2.1. Crystallinity (XRD)

Out of the five tested catalysts, three of them were selected for further structural and morphological characterizations, namely Ni/Ce (with Ni supported on unmodified CeO_2), Ni/Pr10Ce (with Ni supported on CeO_2 modified with 10 at% Pr) and Ni/Pr50Ce (with Ni supported on CeO_2 modified with 50 at% Pr). The crystalline nature of the supports and reduced catalysts was evaluated using XRD and the results are presented in Fig. 4. All the supports and reduced catalysts present the typical reflections attributed to the cubic fluorite lattice of CeO_2 (JCPDS card no: 96-900-9009). The four main reflections of the CeO_2 structure can be found at around 2θ = 28.6°, 33.0°, 47.3° and 56.3°, which correspond to the (111), (200), (220) and (311) lattice planes of crystalline CeO_2. The reduced catalysts present additional reflections at 2θ = 44.6° and 52.0°, which correspond to the (111) and (200) lattice planes of metallic Ni (JCPDS card no: 4-850).

Regarding the prepared Pr-doped CeO_2 supports, Fig. 4(b) focusses on 2θ = 27.0°–31.0°, i.e., on the region of the (111) reflection of CeO_2. It can be clearly observed that an increase in the Pr content in the support leads to a gradual shift of the (111) reflection of CeO_2 towards lower diffraction angles. As a result, the d_{111} spacing is increased from around 3.10 Å for Ce to 3.13 Å for Pr50Ce, meaning that a lattice expansion of the CeO_2 structure occurs upon Pr doping. Therefore, it can be concluded that Pr is rather aliovalently incorporated in the CeO_2 structure in the form of Pr^{3+}, which has an ionic radius larger than that of Ce^{4+} (1.27 and 0.97 Å respectively) [21], causing the formation of oxygen vacancies (Eq. (2)). Moreover, the incorporation of Pr^{3+} into CeO_2 causes a shrinkage of the CeO_2 crystallite size from 10 nm for Ce, down to 5 nm for Pr50Ce (broadening of the (111) CeO_2 reflection) (Table 2). It has been previously reported by Borchert et al. [32], that in Pr-doped CeO_2 with high Pr contents (>10 at%), Pr tends to segregate at the surface and grain boundaries, thereby hindering the further growth of the CeO_2 nanocrystals.

Regarding the reduced catalysts, the most noticeable difference between the X-ray diffractograms is the broadening of the (111)

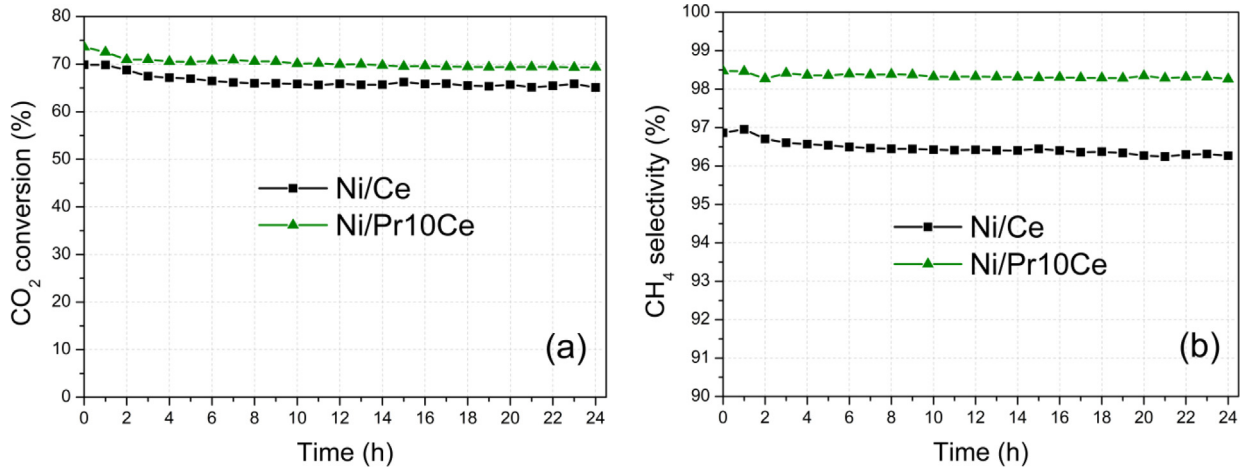

Fig. 3. Catalytic performance for the Ni/Ce and Ni/Pr10Ce catalysts at a steady temperature of 400 °C as a function of reaction time: (a) CO_2 conversion and (b) CH_4 selectivity. Reaction conditions: Experimental Protocol #3 (WHSV = 25000 mL $g_{cat}^{-1}h^{-1}$).

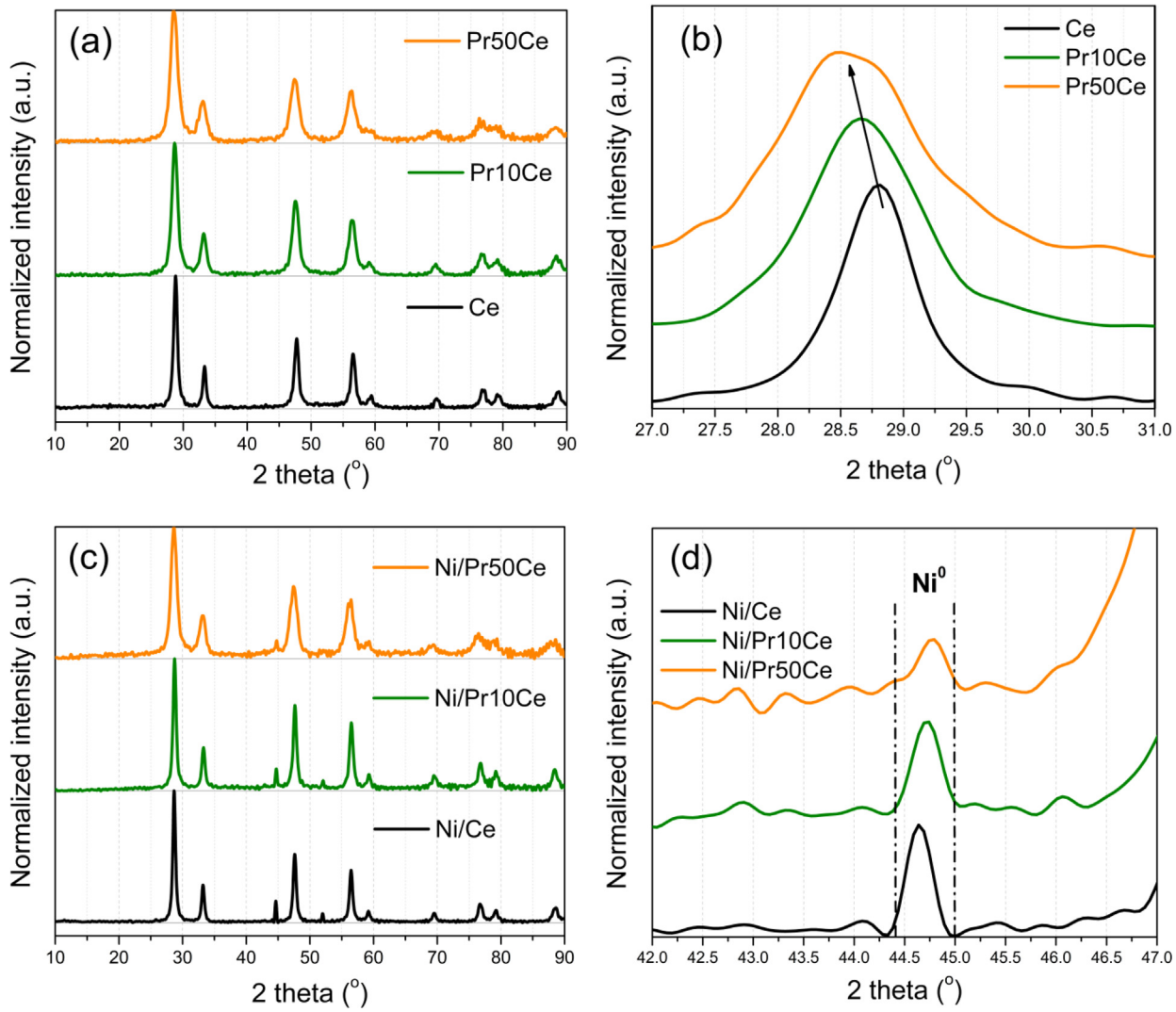

Fig. 4. (a and b) X-ray diffractograms of the Ce, Pr10Ce, and Pr50Ce prepared supports. (c and d) X-ray diffractograms of the Ni/Ce, Ni/Pr10Ce, and Ni/Pr50Ce reduced catalysts.

Table 2
(111) CeO_2 reflection position (2θ) determined via XRD, as well as CeO_2 and Ni^0 crystallite sizes calculated with the help of the Scherrer equation (for the most intense (111) reflections of CeO_2 and metallic Ni). Values correspond to the supports, while the values for the reduced catalysts can be found in parentheses.

Sample name	(111) CeO_2 reflection position, 2θ (°)	CeO_2 d_{111} spacing (Å)	CeO_2 crystallite size (nm)	Ni^0 crystallite size (nm)[a]
Ce (Ni/Ce)	28.8 (28.8)	3.10 (3.10)	10 (14)	31
Pr10Ce (Ni/Pr10Ce)	28.7 (28.8)	3.12 (3.10)	7 (12)	19
Pr50Ce (Ni/Pr50Ce)	28.5 (28.6)	3.13 (3.11)	5 (7)	11

[a] Values correspond to the reduced catalysts.

reflection of metallic Ni (Fig. 4d focusses on the region of the (111) Ni^0 reflection). As a result, the crystallite size of metallic Ni calculated with the help of the Scherrer equation drops considerably from around 31 nm for Ni/Ce, down to around 11 nm for Ni/Pr50Ce. Thus, the incorporation of Pr^{3+} into the CeO_2 support, along with the possible segregation of PrO_x at the support grains [32], clearly exerts a positive influence regarding the dispersion of the catalytically active Ni phase. A similar phenomenon, namely a decrease of the Ni crystallite size upon Pr doping of the CeO_2 support, was also reported by Xiao et al. [24]. It should also be noted, that the position of the (111) reflection of CeO_2 in some reduced catalysts is slightly shifted towards higher diffraction angles compared to the corresponding supports, as a result of some Ni^{2+} cations (ionic radius of 0.55 Å) entering the $Ce_{1-x}Pr_xO_{2-\delta}$ solid solution and causing a shrinkage of the support lattice [33]. In short, the most significant difference between the catalysts with different Pr contents is the reduction in the crystallite size of the CeO_2 support and metallic Ni by increasing the Pr at% in CeO_2. The data extracted from XRD characterization can be found in Table 2.

3.2.2. Textural properties (N_2 physisorption)

The physisorption isotherms and the pore size distributions for the three reduced catalysts can be found in Fig. 5. The isotherms can be classified as Type IV, which are typical of mesoporous materials, whereas the hysteresis loops can be assigned to type H3, which can be found in solids consisting of non-rigid, plate-like par-

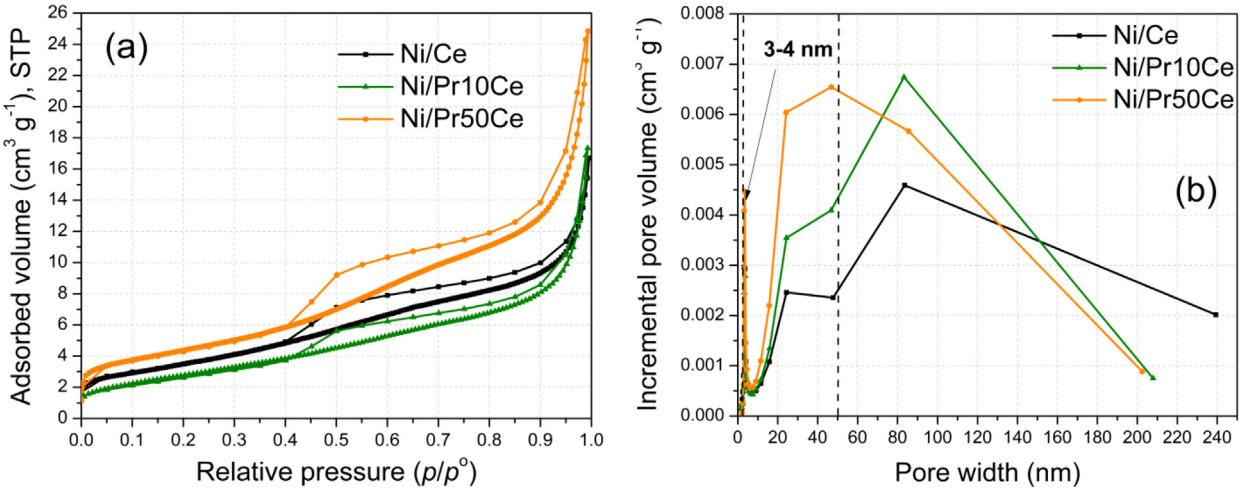

Fig. 5. (a) Physisorption isotherms and (b) pore size distributions for the Ni/Ce, Ni/Pr10Ce, and Ni/Pr50Ce reduced catalysts.

ticles [34]. The BET surface area was calculated at 11, 8 and 14 m^2 g^{-1}, the pore volume at 0.02, 0.03 and 0.04 cm^3 g^{-1} and the average pore width at 8, 13 and 10 nm for Ni/Ce, Ni/Pr10Ce and Ni/Pr50Ce respectively (Table 3). Pore size distribution suggests that the pore structure involves a high number of small mesopores (3–4 nm), as well as larger mesopores (20–50 nm) and macropores (>50 nm). When comparing the different catalysts, it can be observed that Ni/Pr10Ce has a slightly lower BET surface area, whereas a high Pr content in Ni/Pr50Ce increases the porosity of the sample, as a result of the support (CeO_2) and Ni^0 crystallite sizes being much smaller in this case, thereby leading to a reduced pore blockage by the small metallic Ni nanoparticles [35].

3.2.3. Reducibility (H_2-TPR)

H_2-TPR profiles of the calcined catalysts can be found in Fig. 6 (a). In general, these profiles can be separated into three different reduction regions. At low temperatures, i.e., below 250 °C (region I), the reduction of highly dispersed NiO species could lead to the appearance of small reduction peaks [15,18]. Afterwards, centered around 300 °C (region II), the main reduction event that occurs is ascribable to the reduction of the majority of NiO nanoparticles into metallic Ni ones [15,17,18]. Finally, at temperatures higher than 400 °C (region III), the small reduction peaks that emerge can be assigned to the reduction of some oxidized Ni species that interact strongly with the support, as well as the removal of oxygen from the support bulk, which is expected to occur at temperatures higher than 600 °C [17,18,36]. The removal of surface oxygen from the Pr-doped CeO_2 support could occur at temperatures falling in either region II or region III, depending on parameters such as the available surface area and spillover H_2 from metallic Ni [31]. Therefore, part of the support surface oxygen reduction could coincide with the appearance of the large NiO reduction peak in region II, while surface and bulk oxygen reduction in Pr-doped CeO_2 account for some of the H_2 consumption peaks observed at $T > 350$ °C in Fig. 6(a).

When comparing the reducibility of the different catalysts, it is apparent that the reduction of NiO species occurs at elevated temperatures for the catalysts whose support was modified with Pr. In particular, the shift towards higher reduction temperatures is most apparent for NiO/Pr10Ce (maximum of the main reduction peak at 307 °C, compared to 283 °C for NiO/Ce), indicating that the metal-support interaction is stronger in this case [17]. For NiO/Pr50Ce, the main reduction peak shifts again slightly towards lower temperatures, since a potentially stronger metal-support interaction induced by Pr-doping is outweighed by the fact that NiO nanoparticles are much smaller in this case, and thus easier to reduce [15]. At the high temperature region (region III), the reduction peaks appear to be larger for NiO/Pr10Ce and NiO/Pr50Ce compared to NiO/Ce, indicating that the incorporation of Pr into the lattice of CeO_2 can promote the reducibility of the metal oxide support [21,24]. In short, H_2-TPR profiles suggest that an increase of the Pr-content in the support can act to enhance its reducibility and the interaction with the catalytically active Ni phase [17,24].

3.2.4. Surface basicity (CO_2-TPD)

CO_2-TPD (Fig. 6b) has been carried out in order to examine the surface basic properties of the reduced catalysts and thus, their propensity for CO_2 activation [18]. CO_2 can be adsorbed on many different sites of a material in the form of monodentate, bidentate or polydentate carbonates [37]. On metallic Ni sites for example, CO_2 is typically adsorbed either as monodentate/bidentate carbonate, or as CO via the dissociative adsorption of CO_2 to CO^* and O^* [38]. On the surface of the CeO_2 lattice, CO_2 is mostly adsorbed via a monodentate carbonate configuration, followed by O-C-O angle stretching and C-O bond elongation [39]. CO_2 is reported to

Table 3
BET surface area, pore volume and average pore width determined via N_2 physisorption for the reduced catalysts. Temperature at the maximum of the main NiO reduction peak found in H_2-TPR profiles of the calcined catalysts. Ni dispersion and crystallite size calculated via H_2-TPD.

Sample name	BET surface area (m^2 g^{-1})[a]	Pore volume (cm^3 g^{-1})[a]	Average pore width (nm)[a]	T_{max} during H_2-TPR (°C)[b]	Ni dispersion (%)[a]	Ni^0 particle size (nm)[a]
Ni/Ce	11	0.02	8	283	3.0	33
Ni/Pr10Ce	8	0.03	13	307	4.3	23
Ni/Pr50Ce	14	0.04	10	301	5.7	17

[a] Values correspond to the reduced catalysts.
[b] Values correspond to the calcined catalysts.

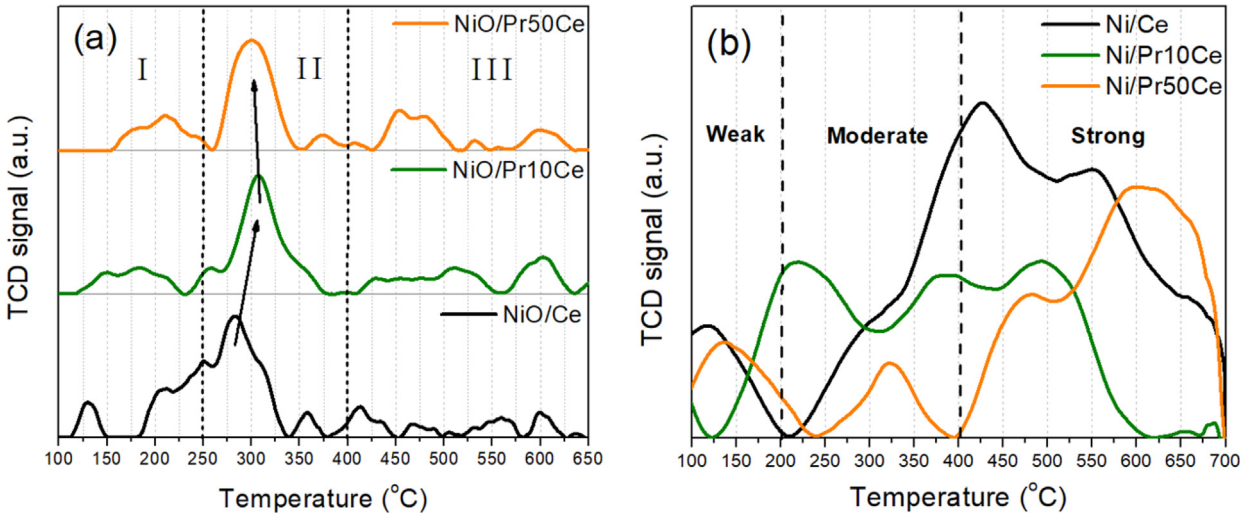

Fig. 6. (a) H_2-TPR profiles of the NiO/Ce, NiO/Pr10Ce, and NiO/Pr50Ce calcined catalysts and (b) CO_2-TPD profiles of the Ni/Ce, Ni/Pr10Ce, and Ni/Pr50Ce reduced catalysts.

be preferentially adsorbed on the oxygen vacancy sites of the reduced CeO_2 (110) surface, therefore the aliovalent substitution of Ce^{4+} with Pr^{3+}, which increases the population of oxygen vacancies, is also expected to favor the adsorption of CO_2 on the support surface [28,39]. Finally, sites at the interface between the CeO_2-based support and the Ni active phase (NiO-CeO_2 interfacial sites) have been reported by some as the most active towards the chemisorption of CO_2, which is regarded as the first step during the CO_2 methanation reaction [14].

Depending on the temperature region of CO_2 desorption at the CO_2-TPD profiles, the surface basic sites can be classified into three categories, namely as weak (<200 °C), moderate (200–400 °C) and strong (>400 °C) basic sites [18]. In the literature, it is often reported that these sites are not of equal importance during CO_2 methanation. Liu et al. [28] has assigned the higher reactivity of Ni catalysts supported on Ca-modified CeO_2 to the increased population of alkaline sites of intermediate strength, whereas Ma et al. [40] have claimed that rather the weak basic sites are the ones contributing to a higher CO_2 methanation activity.

Regarding our catalysts, Ni/Ce appears to exhibit the highest surface basicity, which however originates mostly due to the contribution of strong basic sites. Ni/Pr50Ce also exhibits an increased population of strong basic sites, which could be attributed to the segregation of basic PrO_x and $Pr(OH)_3$ phases at the support grains [32]. On the other hand, NiPr10Ce contains the highest population of alkaline sites of weak and moderate strength, which are the ones often regarded as the most favorable for CO_2 activation during the CO_2 methanation reaction [28,40]. This is possibly a result of the rich defect chemistry of the support and the favorable metal-support interface in this catalyst. CO_2 desorbed from the metallic Ni surface could also contribute to the total basicity of the catalysts [38]. However, as can be seen from the XPS results in Table S1, which will be discussed later, the entirety of Ni is not reduced to its metallic state, as metallic and oxidized Ni species coexist in the reduced catalysts.

3.2.5. Ni dispersion (H_2-TPD)

In order to calculate the Ni dispersion and to provide a mean value for the size of the Ni^0 nanoparticles, H_2-TPD experiments were carried out (Fig. S2). In general, two types of desorbed hydrogen species can be observed during H_2-TPD, namely the ones weakly bonded to the Ni^0 nanoparticles (desorbed at low temperatures, below 200/250 °C) and the ones that are more strongly adsorbed, and thus exhibit a stronger Ni-H binding (desorbed at higher temperatures) [23,41]. In our case, most of the hydrogen is desorbed at low temperatures for Ni/Pr10Ce and Ni/Pr50Ce, whereas a considerable amount of hydrogen is desorbed at higher temperatures for Ni/Ce. The H_2 uptake volume was used to calculate the Ni dispersion and mean Ni^0 particle size, with the corresponding values being presented in Table 3. The H_2-TPD calculated values for Ni^0 particle size appear slightly larger, when compared to the ones calculated via the Scherrer equation (Table 2). This could be explained by the fact that CeO_2 has been reported to partially cover the metallic Ni surface following a high temperature reduction treatment, thereby slightly limiting the availability of potential hydrogen chemisorption sites [42].

3.2.6. Raman analysis

Fig. 7 presents the Raman spectra of the Ce, Pr10Ce and Pr50Ce prepared supports and the Ni/Ce, Ni/Pr10Ce and Ni/Pr50Ce reduced catalysts. All the spectra present the CeO_2 dominant peak at 465 cm^{-1}, that is characteristic of the F_{2g} mode of the CeO_2 fluorite crystal structure. This band, as we move from the ceria to the doped ceria supports, presents a red shift from around 463 cm^{-1} (for Ni/Ce) to 458 cm^{-1} (for Ni/Pr10Ce) and to 445 cm^{-1} (for Ni/Pr50Ce), which is observed both for the supports (Fig. 7a) and the reduced catalysts (Fig. 7b), as well as an asymmetrical broadening in comparison with the undoped counterparts (Ce and Ni/Ce respectively). The shift to lower frequency is due to the lattice expansion originating from the Pr^{3+} cation incorporation into the CeO_2 lattice, though the increase of Pr content up to 50 at% led to a much broader Raman band (at 445 cm^{-1}), due to the increased strain. The above-described changes in the F_{2g} band with varying contents of Pr show that Pr^{3+} has been successfully integrated into the CeO_2 lattice and that solid solutions have formed [43–45].

Focusing next to the defects' region in the Raman spectra of the reduced catalysts, two bands are of importance to be discussed, namely the ones positioned at around 540 and 600 cm^{-1}. These bands are related to the different oxygen vacancy complexes (O_V) local vibrations. The mode at 600 cm^{-1} has its origin in the presence of Ce^{3+}– O_V entities in the CeO_2 lattice. This is the so-called intrinsic vacancy band, and it appears for the Ni/Ce catalyst [46]. The extrinsic vacancy band is present in the Pr-doped samples and is observed due to the oxygen vacancy entities formed by aliovalent doping (Eq. (2)) and/or some hetero-phase oxides (e.g., Pr_6O_{11}). Increasing the Pr content leads to an increase in the intensity of the extrinsic vacancy peak, suggesting an increase in the population of extrinsic vacancies. Deconvolution of this peak at

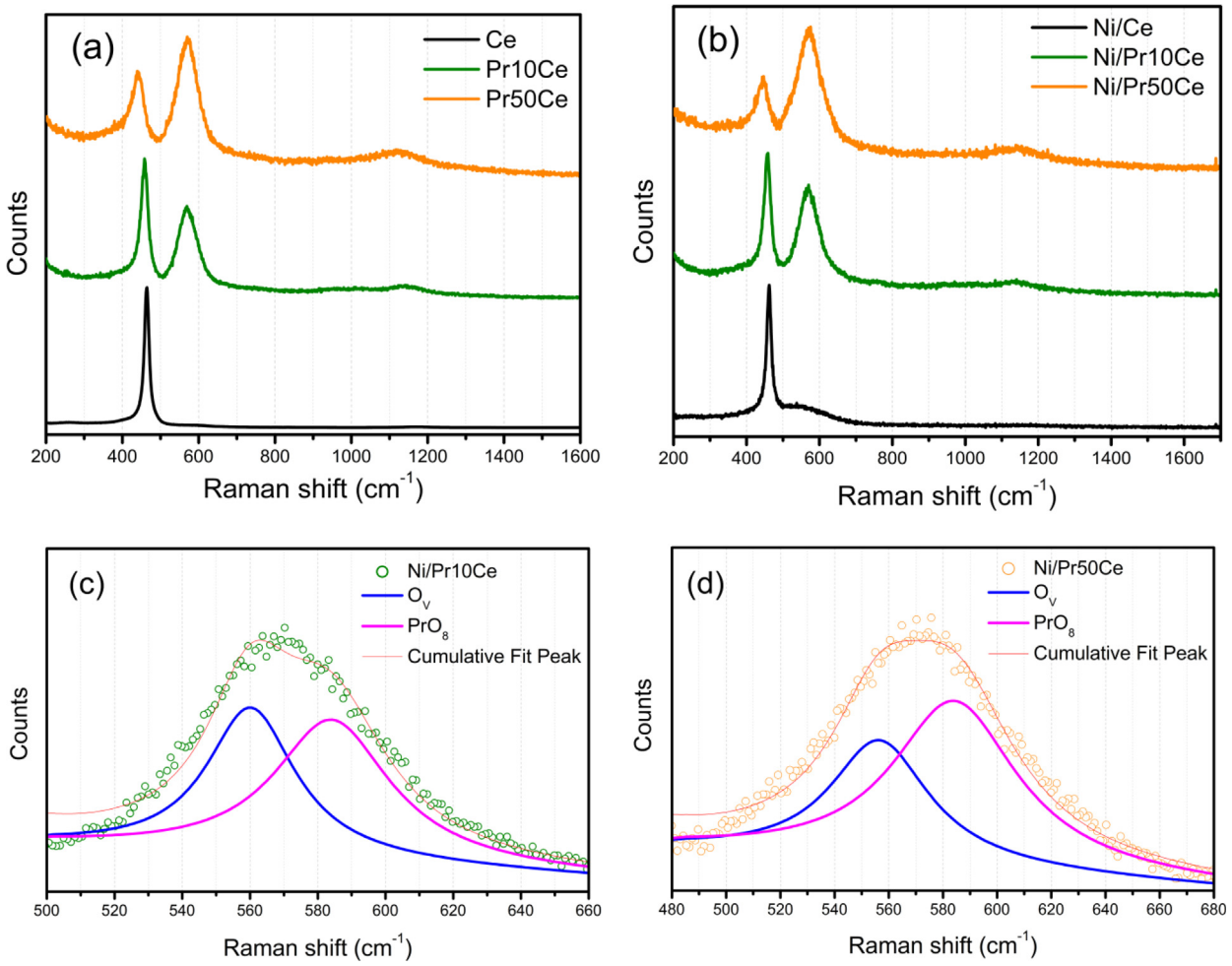

Fig. 7. Raman spectra of (a) the Ce, Pr10Ce, and Pr50Ce prepared supports and (b) Ni/Ce, Ni/Pr10Ce, and Ni/Pr50Ce reduced catalysts. (c and d) Deconvoluted Raman spectra of the Ni/Pr10Ce and Ni/Pr50Ce reduced catalysts.

the defect region (Fig. 7c and d) allows us to evaluate the presence of the hetero phase, as well as the population of the O_V through the ratios of PrO_8/O_V and O_V/F_{2g}. The ratio of O_V/F_{2g} is higher in the case of Ni/Pr10Ce (Fig. 7c) compared to the Ni/Pr50Ce (Fig. 7d) and this is because the low Pr content is almost entirely incorporated into the CeO_2 lattice. On the other hand, in the case of Ni/Pr50Ce with a high Pr concentration, a new phase (likely resembling Pr_6O_{11}) is formed; the latter is corroborated by the PrO_8/O_V ratio as well. Therefore, it can be concluded that Ni/Pr10Ce presents the highest population of oxygen vacancies, which most likely contribute to its improved CO_2 methanation performance.

3.2.7. Surface analysis (XPS)

XPS analyses were carried out ex situ for the reduced catalysts, i.e., after exposure to atmospheric conditions. Fig. 8 presents the Ni 2*p*, Ce 3*d*, O 1*s* and Pr 3*d* core level XPS spectra of the reduced catalysts. The surface elemental composition is presented in Table S1. In general, a higher concentration of Ni than anticipated was detected, caused by Ni preferentially residing at the surface as nanoparticles [18]. The Ni concentration was found to be the highest for Ni/Ce, that contains larger Ni nanoparticles, and the lowest for Ni/Pr50Ce, where Ni nanoparticles are much more well-dispersed and possibly partially encapsulated by CeO_2 and PrO_x [31,42]. Finally, the surface concentration of Pr was also higher than anticipated, which can be attributed to the preferential concentration of Pr'_{Ce} defects at the metal oxide support surface, as well as to the segregation of some PrO_x species [32].

The Ni 2*p* spectra can be found in Fig. 8(a). In general, the peak-shape of the Ni 2*p* peaks indicates the presence of three main types of Ni species. Metallic Ni^0 accounts for the low binding energy (BE) peak centered around 852.7 eV, whereas the other two peaks (~854.3 and ~856.3 eV) correspond to oxidized Ni species [18,31]. Among the two peaks attributed to oxidized Ni species, the low BE one (~854.3 eV) accounts for NiO species and the high BE one (~856.3 eV) can be attributed to Ni-O-Ce interfacial sites, $Ni(OH)_2$ species, or even Ni_2O_3, i.e., Ni^{3+} species due to "defects" in NiO [17,31,47]. Cárdenas-Arenas et al. [14,31] have claimed that the Ni-O-Ce interfacial sites are those most active for the initial step of CO_2 dissociation, whereas metallic Ni^0 sites are active for H_2 dissociation. Although the contribution of Ni-O-Ce sites appears similar in all three reduced catalysts, that for metallic Ni^0 is not. This can be explained by the fact that metallic Ni nanoparticles are larger for the Ni/Ce catalyst and thus less prone to be oxidized under atmospheric conditions, or be encapsulated by CeO_2 or PrO_x, whereas smaller nanoparticles (e.g., in Ni/Pr50Ce) can be more easily oxidized to NiO upon exposure to air [31,42].

Ce 3*d* peaks were labelled according to the nomenclature used in other XPS papers on CeO_2 [48] (Fig. 8b). Peaks labelled as v correspond to Ce $3d_{5/2}$ and those labelled as u to Ce $3d_{3/2}$ transitions respectively [33]. Different peaks are assigned to CeO_2 (Ce^{4+}) and Ce_2O_3 (Ce^{3+}) oxides, with v, v″, v‴, u, u″, u‴ being attributed to

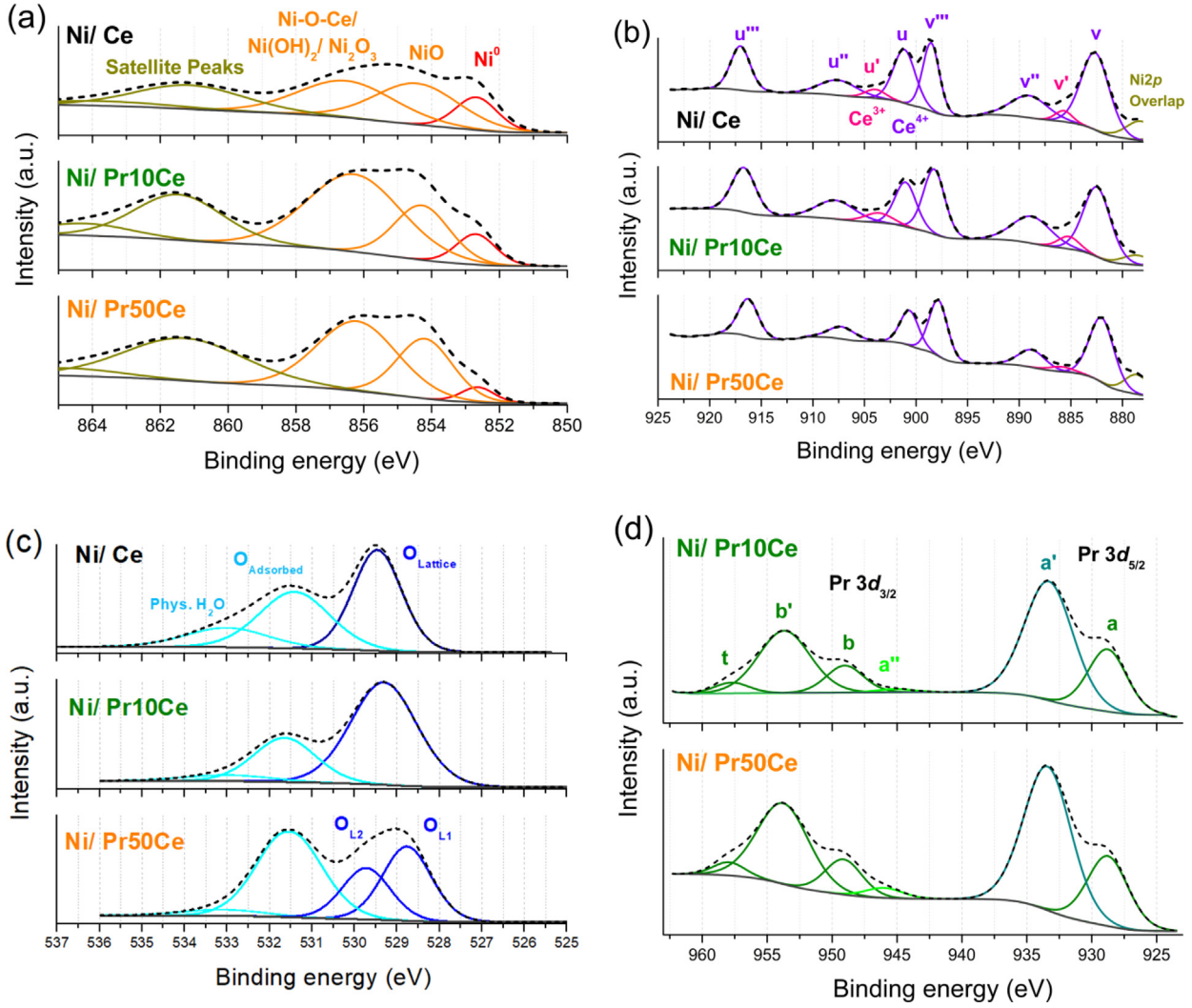

Fig. 8. XPS core level spectra of the Ni/Ce, Ni/Pr10Ce, and Ni/Pr50Ce reduced catalysts. (a) Ni 2*p*, (b) Ce 3*d*, (c) O 1*s*, and (d) Pr 3*d*.

Ce^{4+} and v′, u′ to Ce^{3+} [18,33,48]. Based on peak deconvolution and peak area integration, the percentage of Ce^{3+} species ($Ce^{3+}/(Ce^{4+} + Ce^{3+})$) could be roughly estimated in the range of 2%–7% (5% for Ni/Ce, 7% for Ni/Pr10Ce and just 2% for Ni/Pr50Ce). It should be mentioned, that oxygen vacancies (V_O) in the Pr-doped catalysts are expected to be generated both through the introduction of Pr^{3+} dopants onto Ce^{4+} sites (Pr'_{Ce} defects), and the creation of intrinsic Ce^{3+} species (Ce'_{Ce} defects) [20,21,49]. Besides the extrinsic V_O defects due to the Pr'_{Ce} substitutional impurities, the incorporation of Pr^{3+} in Ni/Pr10Ce appears to also slightly increase the population of Ce^{3+} species (Ce'_{Ce}), which is probably a result of the increased reducibility and oxygen mobility in the 10% Pr-doped support [21]. On the other hand, the population of Ce'_{Ce} defects drops considerably for Ni/Pr50Ce, due to the higher presence of Pr'_{Ce} substitutional impurities and surface PrO_x, which can suppress the $Ce^{4+} \rightarrow Ce^{3+}$ transition [32].

The O 1*s* peaks (Fig. 8c) show the presence of different oxygen species. With increasing binding energies these can be attributed respectively to lattice oxygen, adsorbed oxygen species, like loosely bound oxygen adsorbed on oxygen vacancies, and physisorbed water [17,50,51]. However, the presence of some metal hydroxides/carbonates, as well as superoxide species at higher binding energies cannot be excluded. For Ni/Pr50Ce, the lattice oxygen peak could be further deconvoluted into two separate peaks (O_{L1} and O_{L2}), the higher BE peak corresponding to lattice O^{2-} in the Pr_2O_3-CeO_2 solid solution, and the lower BE one to O^{2-} surrounded by Pr atoms (i.e., PrO_8 coordination around surface Pr'_{Ce} defects or in PrO_x segregated phases).

Lastly, the Pr 3*d* peaks (Fig. 8d) in both Pr-containing catalysts closely resemble the XPS spectrum of Pr_2O_3 rather than that of PrO_2 or Pr_6O_{11}, proving that Pr mainly exists in the catalysts in the form of Pr^{3+} [32,52]. This observation agrees with the XRD results, as well as other literature works [21,32], where Pr is found to dissolve in CeO_2 as Pr^{3+} rather than Pr^{4+}. The peak position of the Pr 3*d* peaks shifts slightly towards higher BE for Ni/Pr50Ce, meaning that this catalyst contains a slightly higher amount of Pr^{4+} species, mostly as segregated PrO_x (Pr_6O_{11}) [32,52]. Though the determination of the percentage of Pr^{3+}:Pr^{4+} ions is challenging, Borchert at al. [32] attempted the deconvolution of the Pr 3*d* peaks into the components a, a′, b and b′ assigned to both Pr^{3+} and Pr^{4+}, a″ assigned exclusively to Pr^{4+} and t, which is an additional feature explained by the multiple effect. They provided a formula for the determination of Pr^{3+}, which takes into account the peak areas of the a′ and a″ peaks. In our case, the a″ (945.7–946.7 eV) peak could only just be observed in Ni/Pr10Ce and its intensity is also small in Ni/Pr50Ce. Therefore, the percentage of Pr^{3+} was calculated at 93% in Ni/Pr10Ce and 80% in Ni/Pr50Ce; the remaining 7% and 20% of

Pr^{4+} respectively could reside as surface-segregated PrO_x (Pr_6O_{11}) [32]. This behavior is to be expected, considering that the catalysts were previously reduced under an H_2 atmosphere, thereby easily converting the majority of Pr species into Pr^{3+} [20].

3.2.8. Electron microscopy analysis

HAADF-STEM images and EDS spectra from selected areas of the Ni/Ce, Ni/Pr10Ce and Ni/Pr50Ce reduced catalysts, as well as EDS mapping for the elements of O, Ni, Ce and Pr in the Ni/Pr10Ce reduced catalyst can be found in Fig. 9. The supports consist of aggregates of small Pr-doped CeO_2 crystallites, forming a spongy network. The structure also contains supported Ni nanoparticles with a great variation in size. Some of them are quite small, most of them appear to be around 10–50 nm, while there are many more larger particles that exceed 50 nm in diameter. EDS analysis confirmed the location of Ni nanoparticles. In agreement with the XRD and H_2-TPD findings, the Ni nanoparticles appear to be larger in Ni/Ce and smaller in the reduced catalysts where the CeO_2 support was modified with Pr. EDS elemental mapping was conducted on the reduced Ni/Pr10Ce catalyst (Fig. 9d). The element of Pr appears to be evenly distributed in the support structure, confirming its successful incorporation into the lattice of CeO_2, though some PrO_x segregated spots could still be present [32]. Most of the Ni nanoparticles observed via EDS mapping appear to have a size of around 10–30 nm, whereas a few larger ones (>50 nm) can also be observed. EDS elemental mapping was also performed on the reduced Ni/Ce and Ni/Pr50Ce catalysts (Fig. S3), so as to compare the effect of Pr-doping on the Ni dispersion. In general, the Ni nanoparticles observed via EDS mapping on Ni/Ce (Fig. S3a) appear larger compared to those on Ni/Pr10Ce (Fig. 9d), which agrees with the XRD and H_2-TPD characterization results (Tables 2 and 3). On the other hand, for the Ni/Pr50Ce catalyst (Fig. S3b), a quite high amount of Ni is also dispersed on the mixed metal oxide support, which makes the localization of metallic Ni nanoparticles via EDS mapping more difficult.

3.3. Spent catalysts characterization

The spent catalysts after the CO_2 methanation time-on-stream experiments at 400 °C (i.e., the catalysts tested under Experimental Protocol #3) were characterized using XRD, N_2 physisorption, Raman and TEM, to examine their structural stability. The X-ray diffractograms and TEM images of the spent catalysts are presented in Fig. 10, whereas the N_2 physisorption isotherms/pore size distributions and Raman spectra can be found in Figs. S4 and S5 respectively. Lastly, the data extracted from the characterization techniques are presented in Table S2.

The X-ray diffractograms (Fig. 10a) of the spent catalysts present the typical reflections of CeO_2 and metallic Ni, with only minor differences in the peak positions and peak broadenings when compared to the diffractograms of the reduced catalysts. As a result, the calculated CeO_2 and Ni^0 crystallite sizes differ only slightly when compared to the reduced catalysts (Table S2). Images taken from the TEM microscope (Fig. 10b and c) also reveal a structure similar to that of the reduced catalysts, with Ni nanoparticles supported on the nanocrystalline Pr-doped CeO_2 support. Evidence of extensive carbon deposition (e.g., growth of carbon nanotubes/-nanofibers [53]) was absent in the spent catalysts, though a very thin and porous carbon shell could potentially cover part of the metallic Ni surface, without greatly affecting the catalytic activity [18,19]. No great changes can either be observed regarding the physisorption isotherms and pore size distribution of the spent catalysts (Fig. S4), with their porous structure (i.e., small mesopores along with larger mesopores and macropores) being similar to that of the reduced catalysts. From the Raman spectra of the spent catalysts, it is shown that Ni/Pr10Ce preserves the oxygen vacancy population, even after the reaction. Therefore, we can conclude that possible deactivation effects (e.g., nanoparticle sintering and coke deposition) have little impact on the catalyst structure and CO_2 methanation activity [19].

3.4. Mechanistic investigation via in-situ DRIFTS

In order to investigate the CO_2 methanation mechanism, as well as possible changes in the reaction mechanism induced via Pr-doping of the support, in-situ DRIFTS experiments were conducted over the unmodified Ni/Ce catalyst (Ni/CeO_2) and the most active Ni/Pr10Ce catalyst ($Ni/Ce_{0.9}Pr_{0.1}O_{2-\delta}$). The spectra in the region between 2250 and 900 cm^{-1} can be found in Fig. 11. The main intermediate species observed for Ni/Ce and Ni/Pr10Ce are formates and carbonates, indicating that CO_2 methanation proceeds via the formate pathway, which involves CO_2 activation over the support surface, in agreement with many other works in the literature studying Ni/CeO_2-type catalysts [17,54–57]. Formate intermediates are also observed for both catalysts at the higher wavenumber region (Fig. S6). Additionally, some carbonyl species (linear, bridged and multi-bonded) were detected on Ni/Ce (Fig. 11). It is uncertain however whether these carbonyls, probably formed on the metallic Ni surface, contribute to CH_4 formation via the CO route (also known as dissociative mechanism or RWGS + CO hydrogenation pathway) [55], or if they are desorbed as gaseous CO following RWGS. The higher number of steps involved during the dissociative pathway would render the formation of CH_4 slower, while the presence of adsorbed CO intermediates can lead to their desorption without their further conversion to CH_4 [55]. The desorption of these carbonyls observed at low temperatures (Fig. 11) to gaseous CO for Ni/Ce, would agree with the increased CO selectivity of this catalyst at low temperatures (as observed in Fig. 1b and Fig. 2b).

A comparison of the spectra for both catalysts at 200 and 250 °C can be found in Fig. S7. It can be clearly seen, that the intensity of the bands of intermediate species is much greater for Ni/Ce, while gaseous CH_4 signal can be observed at lower temperatures for Ni/Pr10Ce. Also, carbonyl bands are present in Ni/Ce and absent in Ni/Pr10Ce. We can conclude that both catalysts follow the formate pathway during CO_2 methanation, while carbon intermediate species can be converted faster towards gaseous CH_4 on the Ni/Pr10Ce catalyst, meaning that Pr-doping promotes the CO_2 methanation reaction. Lastly, the formation of intermediate carbonyl species is hindered upon Pr-doping of the support, which appears to accelerate the formation of CH_4 by favoring the dominant formate pathway (associative mechanism) and limiting the competitive adsorption of CO_2 over the same active sites.

3.5. Correlation between physicochemical characteristics and catalytic performance

It is generally accepted, that differences in the CO_2 methanation catalytic activity can be traced back to the physicochemical properties of the catalysts [5]. These include, but are not limited to, metal dispersion, metal-support interaction, reducibility, surface basicity/acidity, defect chemistry and oxygen lability [5,42,58–60]. Regarding the CO_2 methanation reaction, there is a general consensus that the oxygen mobility of the metal-oxide supports plays a major role towards enhancing the catalytic activity, as oxygen intermediates can be easily transported and removed in-situ during the reaction [14,17,58]. The defect chemistry and more specifically, the population of oxygen vacancies, directly influences the oxygen transport capability of the metal oxide support [20,21]. Furthermore, basic sites of intermediate and low strength (e.g., surface oxygen vacancies and metal-CeO_2 interface) are deemed as highly desirable, since they constitute anchor sites for the initial

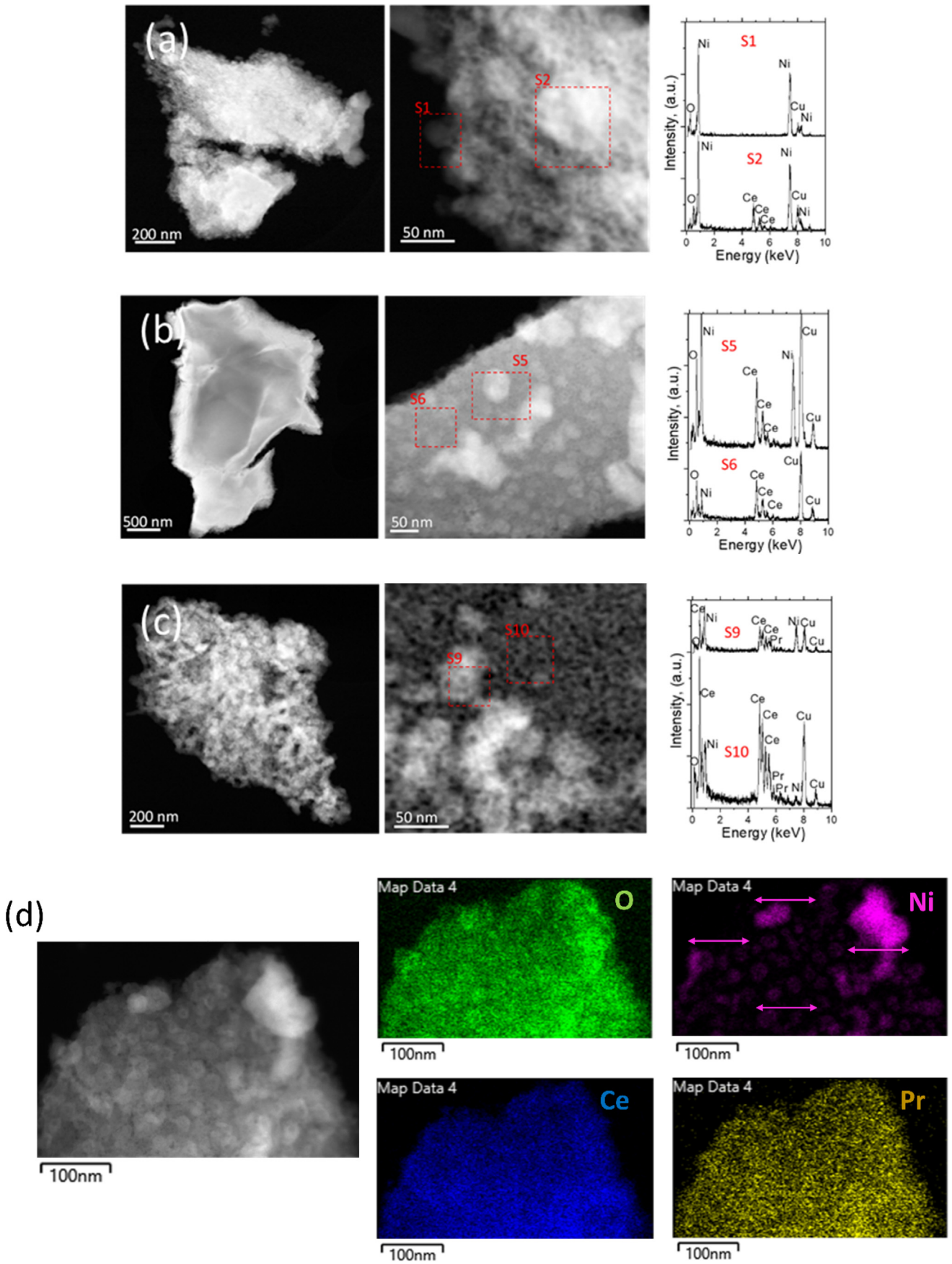

Fig. 9. HAADF-STEM images and EDS spectra of red-dashed marked areas of the (a) Ni/Ce, (b) Ni/Pr10Ce, and (c) Ni/Pr50Ce reduced catalysts. (d) EDS elemental mapping images of the Ni/Pr10Ce reduced catalyst.

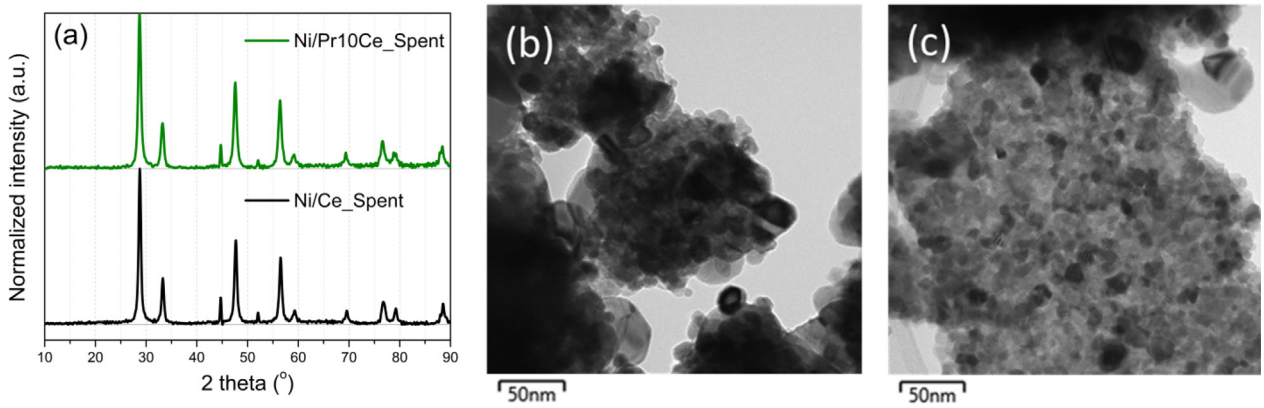

Fig. 10. (a) X-ray diffractograms of the Ni/Ce_Spent and Ni/Pr10Ce_Spent catalysts; TEM images of (b) Ni/Ce_Spent and (c) Ni/Pr10Ce_Spent catalysts (Results obtained for samples tested under Experimental Protocol #3).

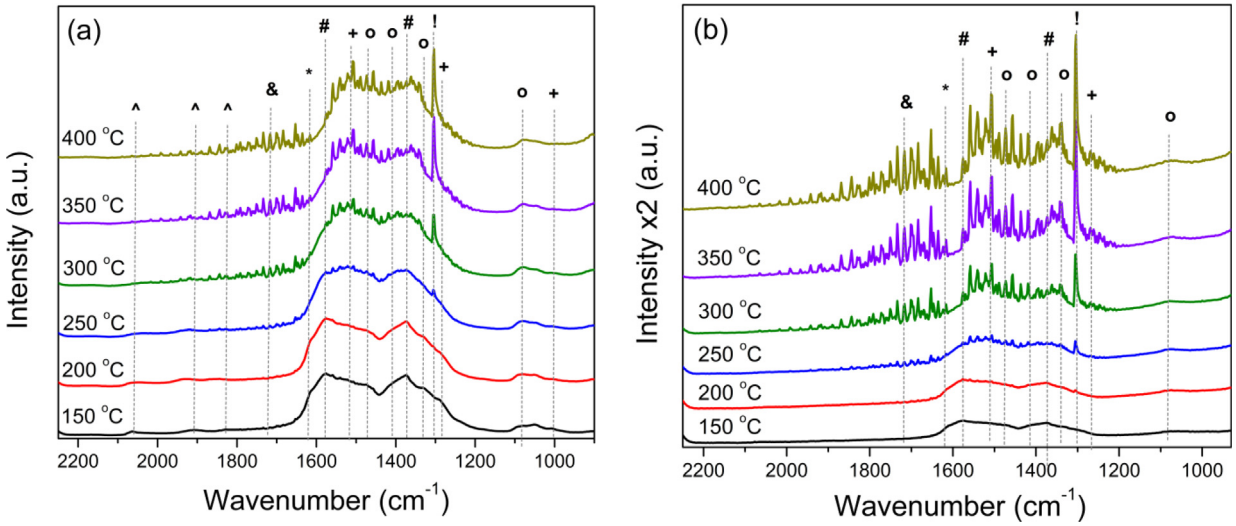

Fig. 11. In-situ DRIFTS spectra of the (a) Ni/Ce and (b) Ni/Pr10Ce (x2 magnification) catalysts. Symbol definition: Linear, bridged and multi-bonded carbonyl (^), formyl (&), bicarbonate (*), formate (#), bidentate carbonate (+), monodentate carbonate (o) and methane (!).

step of CO_2 chemisorption [14,28,40]. Lastly, an easily reducible catalyst is also favored for this reaction, as the metallic surface area of e.g., Ni and Ru is where the H_2 adsorption and dissociation takes place [60].

Among the factors whose role is less clear, is the metal-support interaction and the metal dispersion (i.e., the crystallite size of the catalytically active phase) [30,42,59]. Whereas a high metal dispersion (i.e., small metallic particles) and a strong metal-support interaction are highly desirable in other reactions, such as dry methane reforming, where they can help to mitigate the detrimental effects of carbon accumulation [61], they appear to have a different influence during the CO_2 methanation reaction. Regarding the metal-support interaction, Li et al. [42] reported that, following high-temperature reduction of Ni/CeO_2, a ceria layer can grow on top of the Ni nanoparticles, hampering their catalytic activity. For the metal dispersion, Lin et al. [54] and Marconi et al. [59] claimed that CO_2 methanation over Ni/CeO_2 was favored for the larger Ni nanoparticles over the smaller ones, whereas Varvoutis et al. [30] indicated an optimum Ni nanoparticle size of around 20 nm as the most conducive towards a higher catalytic activity. For Ru-based catalysts (Ru/CeO_2) on the other hand, Ru nanoclusters (1.2 nm) have been reported as more active compared to Ru nanoparticles (4 nm) and Ru single atoms [62].

Based on the existing literature, the catalytic activity enhancement for the 5 at% and 10 at% Pr-doped catalysts, along with the worsening in the performance for the catalysts with higher Pr contents, can be attributed to an interplay between various physicochemical properties and more specifically, the metal nanoparticle size and availability of surface oxygen vacancies. The most active catalyst (Ni/Pr10Ce) exhibits a Ni nanoparticle size of around 23 nm (H_2-TPD), which is very close to the ideal 20 nm proposed by Varvoutis et al. [30]. Higher Pr contents further reduce the particle size of Ni, whereas lower ones boast bigger Ni crystallites, both leading to a change in the ratio of available H_2 and CO_2 chemisorption sites [31]. Oxygen vacancies generally increase in population as the concentration of the extrinsic dopant increases [21]. However, up from a certain degree, further addition of Pr can lead to its segregation on the support grains [32] and to a drop in the oxygen vacancy population (Fig. 7), whereas a compromise of the active Ni-CeO_2 interface may take place, which decreases the available CO_2 chemisorption sites, similarly to the effect of high Pr contents on Ru/CeO_2 [25]. Finally, the population of weak and moderately strong basic sites peaks for the Ni/Pr10Ce catalyst, due to the increased availability of surface oxygen vacancies and the preserved Ni-CeO_2 interface [28,31].

Regarding the active sites contributing to the catalytic activity, it is expected that the high availability of redox surface basic sites

Table 4
Comparison of the catalytic performance of our best-performing 10% Ni/$Ce_{0.9}Pr_{0.1}O_{2-\delta}$ (NiPr10Ce) catalyst with that of other catalysts reported in the literature.

Catalyst	Synthesis method	Reaction conditions	Catalytic performance	Ref.
10% Ni/$Ce_{0.9}Pr_{0.1}O_{2-\delta}$ (Ni/Pr10Ce)	Citrate sol-gel and wet impregnation	WHSV = 25000 mL $g_{cat}^{-1}h^{-1}$ H_2/CO_2 = 4	X_{CO_2} = 72% S_{CH_4} = 98% (T = 400 °C)	This work
10% Ni/CeO_2	Microwave	WHSV = 21000 mL $g_{cat}^{-1}h^{-1}$ H_2/CO_2 = 4	X_{CO_2} = 52% S_{CH_4} = 92% (T = 400 °C)	[65]
10% Ni/CeO_2 (nanopolyhedrons)	Hydrothermal precipitation and Wet impregnation	WHSV = 21000 mL $g_{cat}^{-1}h^{-1}$ H_2/CO_2 = 4	X_{CO_2} = 57% S_{CH_4} = 98.5% (T = 300 °C)	[66]
NiO-CeO_2 (np) (8.5% Ni)	Reversed microemulsion	WHSV = 60000 mL $g_{cat}^{-1}h^{-1}$ H_2/CO_2 = 4	X_{CO_2} = 78% S_{CH_4} = 96% (T = 400 °C)	[67]
10% Ni/CeO_2	Precipitation and excess solvent impregnation	WHSV = 30000 mL $g_{cat}^{-1}h^{-1}$ H_2/CO_2 = 4	X_{CO_2} = 82% S_{CH_4} = 99% (T = 400 °C)	[47]
10% Ni/PrO_x	Precipitation and excess solvent impregnation	WHSV = 30000 mL $g_{cat}^{-1}h^{-1}$ H_2/CO_2 = 4	X_{CO_2} = 78% S_{CH_4} = 99% (T = 400 °C)	[47]
10% Ni/10% Pr_2O_3-CeO_2	Microwave sol-gel and wet impregnation	WHSV = 25000 mL $g_{cat}^{-1}h^{-1}$ H_2/CO_2 = 4	X_{CO_2} = 58% $S_{CH_4}\approx$ 100% (T = 400 °C)	[18]
10% Ni/5% La_2O_3-10% Pr_2O_3-CeO_2	Microwave sol-gel and wet impregnation	WHSV = 25000 mL $g_{cat}^{-1}h^{-1}$ H_2/CO_2 = 4	X_{CO_2} = 57% $S_{CH_4}\approx$ 100% (T = 400 °C)	[19]
10% Ni/CeO_2-ZrO_2 (CeO_2/ZrO_2 = 1.35)	Ammonia evaporation on commercial CeO_2-ZrO_2	WHSV = 20000 mL $g_{cat}^{-1}h^{-1}$ H_2/CO_2 = 4	X_{CO_2} = 55% S_{CH_4} > 99.5% (T = 275 °C)	[68]
10% Ni/$Ca_{0.1}Ce_{0.9}O_x$	Sol-gel and incipient wetness impregnation	WHSV = 36000 mL $g_{cat}^{-1}h^{-1}$ H_2/CO_2 = 4	X_{CO_2} = 75% S_{CH_4} = 99% (T = 290 °C)	[28]

of intermediate and low strength in close proximity to Ni can easily activate the majority of CO_2 molecules, thereby limiting their competitive adsorption with H_2 over metallic Ni (especially for the Pr-promoted catalysts) [12,63]. At the same time, surface metallic Ni sites are able to facilitate the H_2 dissociation and accelerate the complete hydrogenation of adjacently adsorbed carbon intermediates (formates and carbonates) to gaseous methane [14]. Interfacial sites between the active metal and the support (Ni-O-Ce and Ni-O-Pr) could also play a major role during the catalytic reaction by promoting the initial step of CO_2 chemisorption/activation [14,31,64].

Finally, the catalytic activity of our best performing Ni/Pr10Ce catalyst (composition: 10% Ni/$Ce_{0.9}Pr_{0.1}O_{2-\delta}$) is compared with that of other CO_2 methanation catalysts with a similar composition (i.e., similar Ni loading supported on CeO_2, PrO_x or modified CeO_2 supports) used in the literature. The results can be found in Table 4. In general, from the results presented herein, and by also considering other important parameters such as the Ni loading and the WHSV, the catalytic performance of Ni/Pr10Ce compares favorably with many of the studied catalysts, which could be attributed to the rich defect chemistry of the Pr-doped CeO_2 support. A modification of the synthesis procedure to further improve the Ni dispersion in a future work could potentially lead to even better catalytic results.

4. Conclusions

In this work, the effect of aliovalent doping of the CeO_2 support in Ni/CeO_2 catalysts with Pr was investigated. It was found that substituting a small part of Ce^{4+} lattice cations with Pr^{3+} ones (ideally 10 at%) can boost the oxygen vacancy population and decrease the Ni nanoparticle size, thus promoting the availability of active CO_2 and H_2 chemisorption sites. A volcano-type trend was unveiled, where a small degree of Pr doping can increase the catalytic activity and lower the CO_2 activation energy, whereas high Pr loadings can negate the positive effects by instead decreasing the amount of oxygen vacancies and compromising the active Ni-CeO_2 interface due to PrO_x segregation. A 10% increase in CO_2 conversion and a decrease in the CO_2 activation energy from 124 kJ mol^{-1} to 93 kJ mol^{-1} is achieved by modifying the support in Ni/CeO_2 with 10 at% Pr. Moreover, a faster consumption of formate and carbonate intermediates is achieved upon Pr doping. This study proves that aliovalent substitution of CeO_2 with just a small amount of Pr is a valuable tool, which can aid towards the development of highly active Ni-based CO_2 methanation catalysts.

Declaration of Competing Interest

The authors declare that they have no known competing financial interests or personal relationships that could have appeared to influence the work reported in this paper.

Acknowledgements

AIT, NDC and MAG acknowledge support of this work by the project "Development of new innovative low carbon energy technologies to improve excellence in the Region of Western Macedonia" (MIS 5047197) which is implemented under the Action "Reinforcement of the Research and Innovation Infrastructure", funded by the Operational Program "Competitiveness, Entrepreneurship and Innovation" (NSRF 2014-2020) and co-financed by Greece and the European Union (European Regional Development Fund).

Appendix A. Supplementary data

Supplementary data to this article can be found online at https://doi.org/10.1016/j.jechem.2022.04.003.

References

[1] H. Mikulcic, I. Ridjan Skov, D.F. Dominkovic, S.R. Wan Alwi, Z.A. Manan, R. Tan, N. Duić, S.N. Hidayah Mohamad, X. Wang, Renew. Sustain. Energy Rev. 114 (2019) 109338.
[2] A.M. Abdalla, S. Hossain, O.B. Nisfindy, A.T. Azad, M. Dawood, A.K. Azad, Energy Convers. Manag. 165 (2018) 602–627.
[3] J. Gorre, F. Ortloff, C. van Leeuwen, Appl. Energy. 253 (2019) 113594.
[4] K. Ghaib, F.Z. Ben-Fares, Energy Rev. 81 (2018) 433–446.
[5] C. Vogt, M. Monai, G.J. Kramer, B.M. Weckhuysen, Nat. Catal. 2 (2019) 188–197.
[6] A.I. Tsiotsias, N.D. Charisiou, I.V. Yentekakis, M.A. Goula, Catalysts 10 (2020) 812.
[7] U. Bossel, B. Eliasson, Eur. Fuel Cell Forum, Lucerne 36 (2002) 1–35.
[8] W.J. Lee, C. Li, H. Prajitno, J. Yoo, J. Patel, Y. Yang, S. Lim, Catal. Today. 368 (2020) 2–19.
[9] W.K. Fan, M. Tahir, J. Environ. Chem. Eng. 9 (2021) 105460.
[10] A.I. Tsiotsias, N.D. Charisiou, I.V. Yentekakis, M.A. Goula, Nanomaterials 11 (2021) 28.
[11] J. Ren, H. Guo, J. Yang, Z. Qin, J. Lin, Z. Li, Appl. Surf. Sci. 351 (2015) 504–516.
[12] L. Shen, J. Xu, M. Zhu, Y.F. Han, ACS Catal. 10 (2020) 14581–14591.
[13] M.C. Bacariza, D. Spataru, L. Karam, J.M. Lopes, C. Henriques, Processes 8 (2020) 1646.
[14] A. Cárdenas-Arenas, A. Quindimil, A. Davó-Quiñonero, E. Bailón-García, D. Lozano-Castelló, U. De-La-Torre, B. Pereda-Ayo, J.A. González-Marcos, J.R. González-Velasco, A. Bueno-López, Appl. Catal. B Environ. 265 (2020) 118538.
[15] G. Zhou, H. Liu, K. Cui, A. Jia, G. Hu, Z. Jiao, Y. Liu, X. Zhang, Appl. Surf. Sci. 383 (2016) 248–252.
[16] M. Zhu, P. Tian, X. Cao, J. Chen, T. Pu, B. Shi, J. Xu, J. Moon, Z. Wu, Y.F. Han, Appl. Catal. B Environ. 282 (2021) 119561.
[17] Y. Du, C. Qin, Y. Xu, D. Xu, J. Bai, G. Ma, M. Ding, Chem. Eng. J. 418 (2021) 129402.
[18] G.I. Siakavelas, N.D. Charisiou, S. AlKhoori, A.A. AlKhoori, V. Sebastian, S.J. Hinder, M.A. Baker, I.V. Yentekakis, K. Polychronopoulou, M.A. Goula, Appl. Catal. B Environ. 282 (2021) 119562.
[19] G.I. Siakavelas, N.D. Charisiou, A. AlKhoori, S. AlKhoori, V. Sebastian, S.J. Hinder, M.A. Baker, I.V. Yentekakis, K. Polychronopoulou, M.A. Goula, J. CO_2 Util. 51 (2021) 101618.
[20] A.M. D'Angelo, A.L. Chaffee, ACS Omega 2 (2017) 2544–2551.
[21] K. Ahn, D.S. Yoo, D.H. Prasad, H.W. Lee, Y.C. Chung, J.H. Lee, Chem. Mater. 24 (2012) 4261–4267.
[22] Z. Zhang, Y. Wang, J. Lu, J. Zhang, M. Li, X. Liu, F. Wang, ACS Catal. 8 (2018) 2635–2644.
[23] M.M. Makri, M.A. Vasiliades, K.C. Petallidou, A.M. Efstathiou, Catal. Today 259 (2016) 150–164.
[24] Z. Xiao, Y. Li, F. Hou, C. Wu, L. Pan, J. Zou, L. Wang, X. Zhang, G. Liu, G. Li, Appl. Catal. B Environ. 258 (2019) 117940.
[25] S.L. Rodríguez, A. Davó-Quiñonero, J. Juan-Juan, E. Bailón-García, D. Lozano-Castelló, A. Bueno-López, J. Phys. Chem. C 125 (2021) 12038–12049.
[26] L. Pastor-Pérez, E. Le Saché, C. Jones, S. Gu, H. Arellano-Garcia, T.R. Reina, Catal. Today 317 (2018) 108–113.
[27] E. Le Saché, L. Pastor-Pérez, B.J. Haycock, J.J. Villora-Picó, A. Sepúlveda-Escribano, T.R. Reina, ACS Sustain. Chem. Eng. 8 (2020) 4614–4622.
[28] K. Liu, X. Xu, J. Xu, X. Fang, L. Liu, X. Wang, J. CO_2 Util. 38 (2020) 113–124.
[29] Z. Hao, J. Shen, S. Lin, X. Han, X. Chang, J. Liu, M. Li, X. Ma, Appl. Catal. B Environ. 286 (2021) 119922.
[30] G. Varvoutis, M. Lykaki, S. Stefa, V. Binas, G.E. Marnellos, M. Konsolakis, Appl. Catal. B Environ. 297 (2021) 120401.
[31] A. Cárdenas-Arenas, A. Quindimil, A. Davó-Quiñonero, E. Bailón-García, D. Lozano-Castelló, U. De-La-Torre, B. Pereda-Ayo, J.A. González-Marcos, J.R. González-Velasco, A. Bueno-López, Appl. Mater. Today 19 (2020) 100591.
[32] H. Borchert, Y.V. Frolova, V.V. Kaichev, I.P. Prosvirin, G.M. Alikina, A.I. Lukashevich, V.I. Zaikovskii, E.M. Moroz, S.N. Trukhan, V.P. Ivanov, E.A. Paukshtis, V.I. Bukhtiyarov, V.A. Sadykov, J. Phys. Chem. B 109 (2005) 5728–5738.
[33] N. Hashimoto, K. Mori, K. Asahara, S. Shibata, H. Jida, Y. Kuwahara, H. Yamashita, Langmuir 37 (2021) 5376–5384.
[34] M. Thommes, K. Kaneko, A.V. Neimark, J.P. Olivier, F. Rodriguez-Reinoso, J. Rouquerol, K.S.W. Sing, Pure Appl. Chem. 87 (2015) 1051–1069.
[35] C.S. Budi, D. Saikia, C.S. Chen, H.M. Kao, J. Catal. 370 (2019) 274–288.
[36] M. Lykaki, E. Pachatouridou, S.A.C. Carabineiro, E. Iliopoulou, C. Andriopoulou, N. Kallithrakas-Kontos, S. Boghosian, M. Konsolakis, Appl. Catal. B Environ. 230 (2018) 18–28.
[37] S. Ewald, O. Hinrichsen, Appl. Catal. A Gen. 580 (2019) 71–80.
[38] J. Cai, Y. Han, S. Chen, E.J. Crumlin, B. Yang, Y. Li, Z. Liu, J. Phys. Chem. C 123 (2019) 12176–12182.
[39] K.R. Hahn, M. Iannuzzi, A.P. Seitsonen, J. Hutter, J. Phys. Chem. C 117 (2013) 1701–1711.
[40] Y. Ma, J. Liu, M. Chu, J. Yue, Y. Cui, G. Xu, Catal. Lett. 152 (2022) 872–882.
[41] C.M. Damaskinos, M.A. Vasiliades, A.M. Efstathiou, Appl. Catal. A Gen. 579 (2019) 116–129.
[42] M. Li, H. Amari, A.C. van Veen, Appl. Catal. B Environ. 239 (2018) 27–35.
[43] J.R. McBride, K.C. Hass, B.D. Poindexter, W.H. Weber, J. Appl. Phys. 76 (1994) 2435–2441.
[44] M. Guo, J. Lu, Y. Wu, Y. Wang, M. Luo, Langmuir 27 (2011) 3872–3877.
[45] H. Li, G. Lu, Y. Wang, Y. Guo, Y. Guo, Catal. Commun. 11 (2010) 946–950.
[46] Z.D. Dohević-Mitrović, M. Grujić-Brojin, M. Ćepanović, Z.V. Popović, S. Boković, B. Matović, M. Zinkevich, F. Aldinger, J. Phys. Condens. Matter. 18 (2006) 2061.
[47] V. Alcalde-Santiago, A. Davó-Quiñonero, D. Lozano-Castelló, A. Quindimil, U. De-La-Torre, B. Pereda-Ayo, J.A. González-Marcos, J.R. González-Velasco, A. Bueno-López, ChemCatChem 11 (2019) 810–819.
[48] D.R. Mullins, S.H. Overbury, D.R. Huntley, Surf. Sci. 409 (1998) 307–319.
[49] K. Michel, T.S. Bjørheim, T. Norby, J. Janek, M.T. Elm, J. Phys. Chem. C 124 (2020) 15831–15838.
[50] J. Scholz, A. Garbujo, B. Kayaalp, K. Klauke, A. Glisenti, S. Mascotto, Inorg. Chem. 58 (2019) 15942–15952.
[51] H. Ogasawara, A. Kotani, R. Potze, G.A. Sawatzky, B.T. Thole, Phys. Rev. B 44 (1991) 5465.
[52] X. Zhang, L. Liu, J. Feng, X. Ju, J. Wang, T. He, P. Chen, Catal. Lett. 152 (2022) 1170–1181.
[53] N.D. Charisiou, G. Siakavelas, L. Tzounis, V. Sebastian, A. Monzon, M.A. Baker, S. J. Hinder, K. Polychronopoulou, I.V. Yentekakis, M.A. Goula, Int. J. Hydrogen Energy 43 (2018) 18955–18976.
[54] L. Lin, C.A. Gerlak, C. Liu, J. Llorca, S. Yao, N. Rui, F. Zhang, Z. Liu, S. Zhang, K. Deng, C.B. Murray, J.A. Rodriguez, S.D. Senanayake, J. Energy Chem. 61 (2021) 602–611.
[55] A. Solis-Garcia, T.A. Zepeda, J.C. Fierro-Gonzalez, Catal. Today. (2022), https://doi.org/10.1016/j.cattod.2021.10.015 (In Press).
[56] S.M. Lee, Y.H. Lee, D.H. Moon, J.Y. Ahn, D.D. Nguyen, S.W. Chang, S.S. Kim, Ind. Eng. Chem. Res. 58 (2019) 8656–8662.
[57] P. Hongmanorom, J. Ashok, P. Prae Chirawatkul, S. Kawi, Appl. Catal. B Environ. 297 (2021) 120454.
[58] G. Botzolaki, G. Goula, A. Rontogianni, E. Nikolaraki, N. Chalmpes, P. Zygouri, M. Karakassides, D. Gournis, N. Charisiou, M. Goula, S. Papadopoulos, I. Yentekakis, Catalysts 10 (2020) 944.
[59] E. Marconi, S. Tuti, I. Luisetto, Catalysts 9 (2019) 375.
[60] M.A. Arellano-Treviño, N. Kanani, C.W. Jeong-Potter, R.J. Farrauto, Chem. Eng. J. 375 (2019) 121953.
[61] A. Abdulrasheed, A.A. Jalil, Y. Gambo, M. Ibrahim, H.U. Hambali, M.Y. Shahul, Hamid, Renew., Sustain. Energy Rev. 108 (2019) 175–193.
[62] Y. Guo, S. Mei, K. Yuan, D.J. Wang, H.C. Liu, C.H. Yan, Y.W. Zhang, ACS Catal. 8 (2018) 6203–6215.
[63] P.A. Ussa Aldana, F. Ocampo, K. Kobl, B. Louis, F. Thibault-Starzyk, M. Daturi, P. Bazin, S. Thomas, A.C. Roger, Catal. Today 215 (2013) 201–207.
[64] S. Tada, H. Nagase, N. Fujiwara, R. Kikuchi, Energy Fuels 35 (2021) 5241–5251.
[65] S. Ratchahat, S. Surathitimethakul, A. Thamungkit, P. Mala, M. Sudoh, R. Watanabe, C. Fukuhara, S.S. Chen, K.-C.-W. Wu, T. Charinpanitkul, J. Taiwan Inst. Chem. Eng. 121 (2021) 184–196.
[66] T. Jomjaree, P. Sintuya, A. Srifa, W. Koo-amornpattana, S. Kiatphuengporn, S. Assabumrungrat, M. Sudoh, R. Watanabe, C. Fukuhara, S. Ratchahat, Catal. Today 375 (2021) 234–244.
[67] A. Cárdenas-Arenas, H. Soriano Cortés, E. Bailón-García, A. Davó-Quiñonero, D. Lozano-Castelló, A. Bueno-López, Fuel Process. Technol. 212 (2021) 106637.
[68] J. Ashok, M.L. Ang, S. Kawi, Catal. Today 281 (2017) 304–311.